The Astrophysical Journal, 879:90 (17pp), 2019 July 10 https://doi.org/10.3847/1538-4357/ab258f

Comparing Long-duration Gamma-Ray Flares and High-energy Solar Energetic Particles

G. A. de Nolfo[1], A. Bruno[1], J. M. Ryan[2], S. Dalla[3], J. Giacalone[4], I. G. Richardson[1,5], E. R. Christian[1], S. J. Stochaj[6], G. A. Bazilevskaya[7], M. Boezio[8], M. Martucci[9], V. V. Mikhailov[10], and R. Munini[8]
[1] Heliophysics Division, NASA Goddard Space Flight Center, Greenbelt, MD, USA; georgia.a.denolfo@nasa.gov, alessandro.bruno-1@nasa.gov
[2] Space Science Center, University of New Hampshire, Durham, NH, USA
[3] Jeremiah Horrocks Institute, University of Central Lancashire, Preston, PR1 2HE, UK
[4] Department of Planetary Sciences, University of Arizona, Tucson, AZ 85721, USA
[5] Department of Astronomy, University of Maryland, College Park, MD, USA
[6] Electrical and Computer Engineering, New Mexico State University, Las Cruces, NM, USA
[7] Lebedev Physical Institute, RU-119991 Moscow, Russia
[8] INFN, Sezione di Trieste, I-34149 Trieste, Italy
[9] INFN, Sezione di Roma "Tor Vergata," I-00133 Rome, Italy
[10] National Research Nuclear University MEPhI, RU-115409 Moscow, Russia
Received 2019 April 23; revised 2019 May 24; accepted 2019 May 28; published 2019 July 10

Abstract

Little is known about the origin of the high-energy and sustained emission from solar long-duration gamma-ray flares (LDGRFs) identified with the *Compton Gamma Ray Observatory*, the *Solar Maximum Mission*, and now *Fermi*. Though the *Fermi* Large Area Telescope (LAT) has identified dozens of flares with LDGRF signatures, the nature of this phenomenon has been a challenge to explain due to both extreme energies and long durations. The highest-energy emission has generally been attributed to pion production from the interaction of $\gtrsim$300 MeV protons with the ambient matter. The extended duration suggests that particle acceleration occurs over large volumes extending high in the corona, either from stochastic acceleration within large coronal loops or from back precipitation from coronal mass ejection–driven shocks. It is possible to test these models by making a direct comparison between the properties of the accelerated ion population producing the γ-ray emission derived from the *Fermi*/LAT observations and the characteristics of solar energetic particles (SEPs) measured by the *Payload for Matter-Antimatter Exploration and Light Nuclei Astrophysics* spacecraft in the energy range corresponding to the pion-related emission detected with *Fermi*. For 14 of these events, we compare the two populations—SEPs in space and the interacting particles at the Sun—and discuss the implications in terms of potential sources. Our analysis shows that the two proton numbers are poorly correlated, with their ratio spanning more than 5 orders of magnitude, suggesting that the back precipitation of shock-acceleration particles is unlikely to be the source of the LDGRF emission.

Key words: Earth – Sun: coronal mass ejections (CMEs) – Sun: flares – Sun: heliosphere – Sun: particle emission – Sun: X-rays, gamma-rays

1. Introduction

Among the more unusual solar phenomena are the long-duration gamma-ray flares (LDGRFs). The prime feature of these events is delayed and prolonged γ-ray (>100 MeV) emission after the impulsive phase (Ryan 2000). As we discuss below, with the exception of the 2.223 MeV line and other associated emission, there is no clear signal at other wavelengths while this high-energy emission persists. The LDGRF emission is believed to originate from the decay of pions produced by $\gtrsim$300 MeV protons and $\gtrsim$200 MeV α particles. Typically, LDGRFs are associated with fast coronal mass ejections (CMEs) and large solar energetic particle (SEP) events, often exceeding the energies of ground-level enhancements (GLEs; $\gtrsim$500 MeV). However, any direct connection between energetic GLE-type particles observed in space and the accelerated ion population producing the high-energy γ-ray emission is unclear (Cliver 1989).

During the *Solar Maximum Mission* and the *Compton Gamma Ray Observatory* (*CGRO*) mission, only 12 LDGRFs were observed (Forrest et al. 1985; Ryan 2000; Chupp & Ryan 2009). The LDGRFs of 1991 June observed with *CGRO* and GAMMA-1 exhibited nuclear emissions for many hours after the impulsive phase (Akimov et al. 1991; Kanbach et al. 1993; Rank et al. 2001). Notably, the 1991 June 11 flare exhibited emission for nearly 11 hr after the impulsive phase with >50 MeV emission detected with the Energetic Gamma Ray Experiment Telescope (EGRET; Schneid et al. 1994). Mandzhavidze & Ramaty (1992) analyzed the EGRET data for the extended phase of the flare. They found a best fit to the emission spectrum with a combination of pion decay radiation and primary electron bremsstrahlung. However, this was later contraindicated by the Imaging Compton Telescope (COMPTEL) data (Rank et al. 2001) showing the 2.223 MeV neutron-capture line synchronized with the >100 MeV emission, consistent with a 100% nuclear origin.

More recently, the *Fermi* Large Area Telescope (LAT) has observed dozens of LDGRFs (Ackermann et al. 2012, 2014, 2017; Share et al. 2018). These peculiar events share some common characteristics: (1) the extended γ-ray emission is often delayed by several minutes from the impulsive hard X-ray emission and, in some cases, lasts for as long as tens of hr; (2) it appears to lack temporal structure on scales much less than the overall decay time, suggesting that the acceleration takes place over large volumes ($\gtrsim 10^5$ km), smoothing over the details of the dynamics; and (3) the emission is primarily from

high-energy ion interactions, consistent with an origin from π^0 decay (Ackermann et al. 2017). The most intense and longest-duration example of an LDGRF is the 2012 March 7 event, for which >100 MeV emission was observed for nearly 20 hr (Ajello et al. 2014). The long duration of the emission cannot be explained by passive trapping without continued production (such as occurs in the Earth's radiation belts), because even the minutest pitch angle scattering would cause particles to escape into the loss cone on much shorter timescales. To produce a 10 hr particle lifetime in a radiation belt–like loop configuration implies scattering mean free paths of tens of au (Ryan 2000) that are not even observed in the most anisotropic GLE events and would require a magnetic fluctuation level $\delta B/B \sim 0.05$, far quieter than the typical solar wind turbulence.

Several scenarios have been posited to explain the many hours' duration of high-energy emission. These include (1) particle trapping with and without continuous acceleration within large coronal loops, characterized by delayed onset due to the need for ion energies to exceed the pion production threshold (Ryan & Lee 1991; Mandzhavidze & Ramaty 1992; Chupp & Ryan 2009); (2) backward precipitation of particles accelerated at a CME-driven shock (Cliver et al. 1993; Kocharov et al. 2015); and (3) particle acceleration by large-scale electric fields (Akimov et al. 1991, 1996; Litvinenko 2006). Early models considered the injection of particles into large loops with a single phase of acceleration followed by precipitation resulting in the observed γ-ray emission. Murphy et al. (1987) modeled the emission with two particle populations, while Mandzhavidze & Ramaty (1992) included the production of γ-rays from charged pions, the effects of passive particle trapping, and pitch angle scattering into an infinitesimal loss cone. Post-flare loops may provide the magnetic structures necessary for continuous acceleration, in which pitch angle scattering from magnetic turbulence within the loops serves to further accelerate the ion population (Ryan & Lee 1991). Loops of the necessary length appear during the gradual phase of two-ribbon flares and CME liftoff as field line reconnection gives rise to hot flare loops that cool within a few hours. The Hα loops may be as large as 5×10^5 km, creating a system of arches that can last for several hours. Such structures may not be visible in soft X-rays, however. Recent microwave observations from the Expanded Owens Valley Solar Array (EOVSA) suggest the presence of an extended, static loop, with a circular length of 1.4 R_s (Gary et al. 2018), for the 2017 September 10 solar flare that produced significant >100 MeV γ-ray emission.

On the other hand, CME shock–accelerated protons could make their way back from the shock front to the photosphere, radiating γ-rays, as first proposed by Cliver et al. (1993). The CME-driven shocks are widely accepted to accelerate the majority of large gradual SEP events (Reames 1999; Cliver 2016) and, in so doing, transfer typically $\leqslant$10% of the CME kinetic energy to energetic particles (Mewaldt et al. 2008; Aschwanden et al. 2017). The highest-energy events, reaching GeV energies, originate within a few solar radii, where efficient shock acceleration can take place (Zank et al. 2000; Berezhko & Taneev 2003; Lee 2005; Afanasiev et al. 2015). Ng & Reames (2008) showed that GeV energies can be reached within ~10 minutes for a shock speed of 2500 km s^{-1} with typical coronal conditions. Large-scale quiet loops that could efficiently transport particles may connect the shock front (for extended periods) and lead particles back to the photosphere. The idea that the same CME-driven shock is responsible for accelerating SEPs and protons producing LDGRFs is supported by recent studies investigating statistical correlations (Gopalswamy et al. 2018; Winter et al. 2018). However, particle diffusion through the turbulent sheath downstream of the shock is expected to be inefficient; furthermore, the entire particle population is being rapidly convected outward. Kocharov et al. (2015) examined the feasibility of back precipitation and could achieve only up to 1% of GLE particles precipitating back to the Sun. Notably, *Fermi*/LAT observations revealed three behind-the-limb LDGRFs (Ackermann et al. 2017), suggesting a much larger longitudinal extent to the solar source. Plotnikov et al. (2017) investigated the 3D reconstruction of coronal shocks from these backside events and concluded that LDGRF emission begins when the magnetic connectivity to the shock reaches the solar surface facing the Earth. Indeed, the highest fluxes in terms of both LDGRF emission and in situ SEPs were observed for the backside event on 2014 September 1, with the fastest-moving shock. Jin et al. (2018) simulated this event using a global magnetohydrodynamic (MHD) model and also found that particles could escape downstream of the shock along magnetic field lines that connect to the solar surface facing Earth.

A CME-driven shock origin is not without challenges. Hudson (2017) pointed out the importance of magnetic mirroring as particles propagate sunward in preventing back precipitation to the photosphere, consistent with the conclusions of Kocharov et al. (2015). He proposed two alternative scenarios, including the "Lasso" scenario, where particles are trapped in a magnetic structure that subsequently retracts back to the solar surface. The second alternative is a coronal "thick target" scenario, where protons are trapped in a static volume for several hours. Depending on the level of turbulence in this volume, these same particles may be accelerated concomitant with the trapping, extending the potential duration for trapping (Ryan et al. 2018a, 2018b). Grechnev et al. (2018) found the detectable emission from the backside event of 2014 September 1 to be consistent with flare-accelerated particles trapped in static coronal loops and possibly reaccelerated in these loops by a shock wave excited by the initial eruption.

High-energy charged-particle events detected by in situ spacecraft at large distances from the Sun and LDGRFs share similar energy ranges for the protons/ions responsible for them. High-energy SEPs and LDGRFs are due to ions rather than electrons, and both are delayed by several minutes from the associated X-ray event (Kahler et al. 1984; Ryan 2000), suggesting a linkage. A potential association between LDGRFs and GLE-type particles has been investigated, but the results are inconclusive (Ramaty & Murphy 1987; Ryan 2000; Chupp & Ryan 2009; Ackermann et al. 2017). Absent accompanying signals at other wavelengths, understanding the LDGRF emission is difficult. Only a few options seem to survive scrutiny: (1) LDGRFs contribute directly to SEPs, (2) SEPs produce LDGRFs through back precipitation of particles accelerated at the CME-driven shock, and (3) LDGRFs and high-energy SEP events are correlated but not causally (e.g., the two phenomena may be linked to M- and X-class flares but are otherwise separate processes with no exchange of particles).

One way to constrain the possible scenarios is to compare the number of protons interacting at the Sun above the pion production threshold (~300 MeV) inferred from the extended

γ-ray emission with the number of SEPs in space above the same energy. This is now possible for the first time with the *Payload for Matter-Antimatter Exploration and Light Nuclei Astrophysics* (*PAMELA*) and the accompanying γ-ray observations with *Fermi*/LAT. In particular, we calculate the total number of >500 MeV protons at 1 au, N_{SEP}, taking advantage of the *PAMELA* and *Solar Terrestrial Relations Observatory* (*STEREO*) data with the aid of transport simulations, and compare it with the number of high-energy protons at the Sun, N_{LDGRF}, as deduced from *Fermi*/LAT data. The ions producing the emission detected with *Fermi* are in the same energy range as those observed with *PAMELA* (see next section), presenting an opportunity for a proper comparison of the two particle populations, which is key to determining the mechanism responsible for the extended duration of the γ-ray emission.

The paper is structured as follows. In Section 2 we present the SEP observations from *PAMELA* and LDGRF data from *Fermi*/LAT for the events used in our analysis. Section 3 describes how we derived information on the spatial extent of SEP events from combined spacecraft data and how simulations of SEP propagation were used to estimate the number of times particles cross 1 au. Our main results on comparing N_{LDGRF} and N_{SEP} are presented in Section 4 and discussed in Section 5. Finally, Section 6 reports our summary and conclusions.

2. *PAMELA* and *Fermi*/LAT Observations

PAMELA is a space experiment designed to measure the charged cosmic radiation (protons, electrons, their antiparticles, and light nuclei) in the energy range from several tens of MeV up to several hundred GeV. The instrument consists of a magnetic spectrometer equipped with a silicon tracking system, a time-of-flight system shielded by an anticoincidence system, an electromagnetic calorimeter, and a neutron detector. The *Resurs-DK1* satellite carrying the apparatus was launched into a semipolar 70° inclination and elliptical (350–610 km) orbit on 2006 June 15. *PAMELA* provided comprehensive observations of the galactic, solar, and magnetospheric radiation in the near-Earth environment (Adriani et al. 2011, 2014; Bruno et al. 2016a, 2016b; Adriani et al. 2017). The mission lifetime was extended beyond 2015, in part due to the promise of new *PAMELA* SEP science, such as that presented in this paper. On 2016 January 24, the spacecraft lost contact with ground stations. The *PAMELA* team has recently published the detailed spectra of 26 high-energy SEPs between 2006 December and 2014 September (Bruno et al. 2018). These observations span a broad range in energy from ~80 MeV to 1–2 GeV, encompassing both the low-energy measurements of in situ spacecraft and the ground-based observations of the neutron monitor network. The reported spectra are consistent with diffusive shock acceleration with clear exponential rollovers attributed to particle escape from within the shock region during acceleration. The absence of qualitative differences between the spectra of GLE and non-GLE events suggests that GLEs are not a separate class of SEP events but rather are the extreme end of a continuous spectral distribution. The *PAMELA* observations have been used by Bruno (2017) to calibrate the >80 MeV proton channels of the Energetic Proton, Electron, and Alpha Detectors (EPEADs) and the High Energy Proton and Alpha Detectors (HEPADs) on board *GOES-13* and *-15*, bringing the detected spectral intensities in line with those registered by *PAMELA* and thus enabling a more reliable spectroscopic measurement up to ~1 GeV for SEP events occurring during periods when *PAMELA* was not acquiring data or after the mission termination (Bruno et al. 2019).

Fermi/LAT is a pair-conversion telescope with sensitivity to γ-rays between ~20 MeV and 300 GeV (Atwood et al. 2009) and a duty cycle for solar events of only ~15%–20% due to frequent occultation of the Sun by the Earth and passages through the South Atlantic Anomaly (SAA). However, the *Fermi* satellite is able to perform pointed ("target-of-opportunity") observations increasing the exposure to a particular part of the sky, including the Sun. Dozens of LDGRFs have been reported since the launch of the spacecraft on 2008 June 11 (Ackermann et al. 2012, 2014, 2017; Share et al. 2018). To derive events from the data set, a point source is placed at the location of the Sun and a power law with an exponential cutoff is assumed as the best-fit spectral model. All events with photon energies above 100 MeV and directions within 12° of the Sun are included in the analysis. The γ-ray background from the Earth's atmosphere is reduced by restricting the allowable events to zenith angles <100°. A solar flux is obtained using a "maximum likelihood" analysis (https://hesperia.gsfc.nasa.gov/fermi/lat/qlook/max_likelihood/) that compares the likelihood obtained by fitting the data with the solar source included with the likelihood of the null hypothesis (no solar source). Details of the analysis of LAT solar flares were published by Ackermann et al. (2013). The number of protons inferred from the γ-ray emission used in this study relies on the observations of Share et al. (2018) based on a "light-bucket" approach (https://hesperia.gsfc.nasa.gov/fermi/lat/qlook/light_bucket/), implementing a less accurate but faster algorithm to identify intervals of transient excess high-energy solar emission. It should be noted that, with respect to the maximum likelihood method, the background is not fitted, and the exposure is calculated with an assumed spectral model.

Table 1 reports the SEP events with an associated LDGRF detected by *Fermi*/LAT above 100 MeV between 2008 August and 2019 April. The LDGRF list is based on Share et al. (2018), except for events 15, 16, 19, and 20, identified with the maximum likelihood analysis by Winter et al. (2018), and the two events occurring in 2017 (22 and 23), derived from the light-bucket list of LAT observations (https://hesperia.gsfc.nasa.gov/fermi/lat/qlook/lat_events.txt). The first five columns provide the event number, the SEP event onset times (UT), and the event-integrated intensities of protons above 80, 300, and 500 MeV, based on the extrapolation of fits of the *PAMELA* spectra (Bruno et al. 2018); data from *GOES-13/15* are used below 80 MeV to constrain the fits at low energies, based on the mean energies provided by Sandberg et al. (2014). For events not registered by *PAMELA* (the two events on 2011 August, the 2012 March 7 event, and those occurring after 2014), the fits are based on the EPEAD and HEPAD spectral points as described in Bruno et al. (2019), using the mean energies derived by Bruno (2017). The uncertainties on the event-integrated intensities are computed from the covariance matrix of the fits. For the four eruptions occurring in 2012 March (no. 8), a single SEP intensity value is provided. Columns 6–8 list the parent flare onset time (UT), location (degrees), and soft X-ray class from the *GOES* X-ray archive (ftp://ftp.ngdc.noaa.gov/STP/space-weather/solar-data/solar-features/solar-flares/x-rays/goes/). For the 2014 January 6 and September 1 events, originating on the far side of the Sun, the flare size was estimated by Ackermann et al. (2017) from observations made by the Extreme Ultraviolet Imager (EUVI) on board the *STEREO*

Table 1

List of SEP Events with an Associated LDGRF Detected by *Fermi*/LAT above 100 MeV between 2008 August and 2017 September, Based on Share et al. (2018) and Winter et al. (2018)

1	2				3			4		
	SEP Event				Flare			CME		
No.	Onset	>80 MeV	>300 MeV	>500 MeV	Onset	Location	Class	1st App.	Speed	Direction
1	2011 03/07, 21:30	5.4×10^{2}[a]	4.1×10^{-2}[a]	3.4×10^{-4}[a]	03/07, 19:43	N30W48	M3.7	03/07, 20:00	2223	N17W50
2	2011 06/07, 07:00	$(1.5 \pm 0.1) \times 10^{5}$	$(3.9 \pm 0.2) \times 10^{3}$	$(4.9 \pm 0.8) \times 10^{2}$	06/07, 06:16	S21W54	M2.5	06/07, 06:49	1321	S25W52
3[b]	2011 08/04, 08:05	$(4.9 \pm 1.4) \times 10^{4}$	2.5×10^{2}[a]	1.0×10^{1}[a]	08/04, 03:41	N15W39	M9.3	08/04, 04:12	1477	N14W40
4[b]	2011 08/09, 08:05	$(2.8 \pm 0.5) \times 10^{4}$	$(5.1 \pm 2.0) \times 10^{2}$	$(4.5 \pm 4.3) \times 10^{1}$	08/09, 07:48	N17W69	X6.9	08/09, 08:12	1640	S12W62
5	2011 09/06, 23:35	$(1.9 \pm 0.1) \times 10^{4}$	$(7.0 \pm 1.0) \times 10^{2}$	$(1.0 \pm 0.3) \times 10^{2}$	09/06, 22:12	N14W18	X2.1	09/06, 23:05	830	N20W20
6	2012 01/23, 04:20	$(1.5 \pm 0.2) \times 10^{5}$	$(1.3 \pm 0.2) \times 10^{2}$	$(6.1 \pm 3.1) \times 10^{0}$	01/23, 03:38	N28W21	M8.8	01/23, 04:00	2511	N41W26
7	2012 01/27, 18:40	$(5.6 \pm 0.4) \times 10^{5}$	$(1.1 \pm 0.1) \times 10^{4}$	$(2.0 \pm 0.2) \times 10^{3}$	01/27, 17:37	N27W71	X1.8	01/27, 18:27	2541	N40W75
8	2012 03/07, 01:40	$(5.2 \pm 1.1) \times 10^{6}$	$(8.7 \pm 3.0) \times 10^{4}$	$(1.1 \pm 0.4) \times 10^{4}$	03/07, 00:02	N17E27	X5.4	03/07, 00:24	3146	N30E60
					03/07, 01:05	N22E12	X1.3	03/07, 01:30	2160	N04E23
					03/09, 03:22	N16W02	M6.3	03/09, 04:26	1229	N08E25
					03/10, 17:15	N18W26	M8.4	03/10, 18:00	1638	N22E05
9	2012 05/17, 01:50	$(2.9 \pm 0.1) \times 10^{5}$	$(2.0 \pm 0.1) \times 10^{4}$	$(5.3 \pm 0.4) \times 10^{3}$	05/17, 01:25	N11W76	M5.1	05/17, 01:48	1596	S10W75
10	2012 07/07, 00:05	$(1.5 \pm 0.1) \times 10^{4}$	$(2.0 \pm 0.8) \times 10^{2}$	$(1.6 \pm 1.4) \times 10^{1}$	07/06, 23:01	S13W59	X1.1	07/06, 23:24	1907	S35W65
11	2013 04/11, 08:00	$(1.0 \pm 0.1) \times 10^{5}$	$(1.4 \pm 0.2) \times 10^{3}$	$(8.9 \pm 3.1) \times 10^{1}$	04/11, 06:55	N09E12	M6.5	04/11, 07:24	1369	S07E25
12	2013 05/13, 16:30?	7.3×10^{1}[a]	7.3×10^{-6}[a]	...	05/13, 15:48	N10E89	X2.8	05/13, 16:08	1852	N10E70
13	2013 05/15, 02:00?	2.0×10^{2}[a]	2.0×10^{-2}[a]	5.5×10^{-4}[a]	05/15, 01:25	N11E63	X1.2	05/15, 01:48	1408	N15E70
14	2013 10/28, 17:55	$(1.7 \pm 0.1) \times 10^{4}$	$(5.4 \pm 0.9) \times 10^{2}$	$(7.4 \pm 2.5) \times 10^{1}$	10/28, 15:07	S06E28	M4.4	10/28, 15:36	1098	N10E20
15	2014 01/06, 08:05	$(1.0 \pm 0.0) \times 10^{5}$	$(5.0 \pm 0.2) \times 10^{3}$	$(9.4 \pm 0.6) \times 10^{2}$	01/06, 07:30 (a)	S15W112 (b)	~X3.5 (b)	01/06, 08:00	1431	S03W102
16	2014 01/07, 19:20	2.2×10^{5}[a]	1.7×10^{3}[a]	1.9×10^{2}[a]	01/07, 18:04	S15W11	X1.2	01/07, 18:24	2246	S24W30
17	2014 02/25, 03:00	$(1.3 \pm 0.1) \times 10^{5}$	$(4.2 \pm 0.2) \times 10^{3}$	$(8.1 \pm 1.0) \times 10^{2}$	02/25, 00:39	S12E82	X5.0	02/25, 01:25	2153	S11E78
18	2014 09/01, 17:00	$(2.1 \pm 0.1) \times 10^{5}$	$(9.7 \pm 0.7) \times 10^{3}$	$(1.5 \pm 0.6) \times 10^{3}$	09/01, 10:54 (c)	N14E127 (b)	~X2.4 (b)	09/01, 11:12	2017	N01E155
19	2014 09/10, 19:45	$(6.0 \pm 0.4) \times 10^{4}$	$(1.0 \pm 0.1) \times 10^{3}$	1.0×10^{2}[a]	09/10, 17:21	N14E02	X1.7	09/10, 18:00	1652	N15W10
20[b]	2015 06/21, 02:30?	$(7.7 \pm 4.7) \times 10^{2}$	5.9×10^{-1}[a]	3.4×10^{-2}[a]	06/21, 02:06	N13E12	M2.6	06/21, 02:36	1740	N07E08
21[b]	2015 06/25, 09:30	4.4×10^{1}[a]	1.6×10^{-3}[a]	2.9×10^{-5}[a]	06/25, 08:02	N09W42	M7.9	06/25, 08:36	1805	N23W42
22[b]	2017 09/06, 12:20	$(1.8 \pm 0.4) \times 10^{4}$	$(1.3 \pm 0.6) \times 10^{2}$	$(1.9 \pm 1.0) \times 10^{1}$	09/06, 11:53	S08W33	X9.3	09/06, 12:24	1571[c]	S15W23
23[b]	2017 09/10, 16:05	$(4.5 \pm 1.3) \times 10^{6}$	$(1.1 \pm 0.3) \times 10^{5}$	$(2.3 \pm 0.6) \times 10^{4}$	09/10, 15:35	S08W88	X8.2	09/10, 16:00	3163[c]	S12W85

Notes. The first five columns report the SEP event number, onset time (UT), and event-integrated intensities (sr^{-1} cm^{-2}) above 80, 300, and 500 MeV. The question marks indicate uncertain onset times. For the four eruptions occurring on 2012 March (no. 8), a single SEP intensity value is provided. Columns 6–8 indicate the parent flare onset time (UT), location (degrees), and class based on *GOES* soft X-ray data. Columns 9–11 report the associated CME first appearance time (UT) and space speed (km s^{-1}) according to the CDAW catalog and direction (degrees) from the DONKI database. The dots (...) indicate no data available. See the text for details.

[a] Upper limit.

[b] *PAMELA* data not available.

[c] Projected speed (space speed not available).

References. (a) Thakur et al. (2014), (b) Ackermann et al. (2017), (c) Plotnikov et al. (2017).

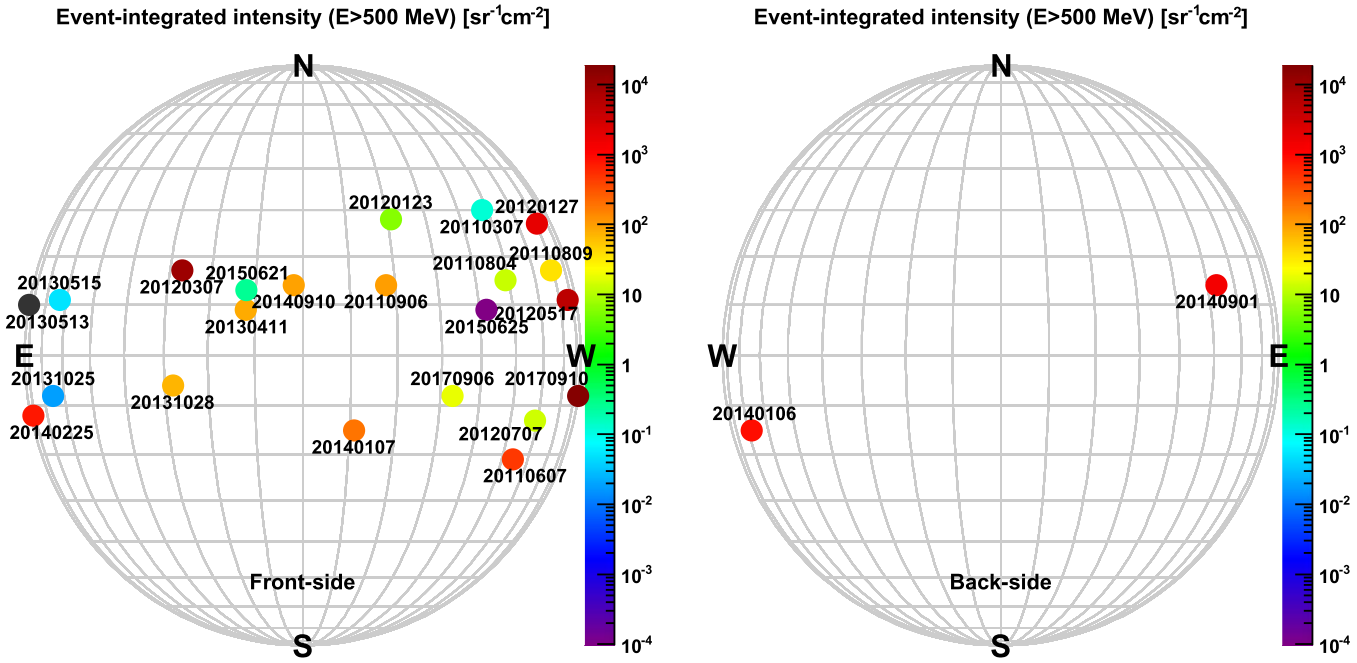

Figure 1. Heliographic locations of parent flares for the SEP events listed in Table 1. Front- and backside events are displayed in the left and right panels, respectively. The color code indicates the SEP event-integrated intensity above 500 MeV; the one event with no signal above this threshold is shown in black.

spacecraft based on the method by Nitta et al. (2013). Columns 9–11 provide the associated CME first appearance time (UT) and space (3D) velocity (km s^{-1}) according to the Coordinated Data Analysis Workshops (CDAW; https://cdaw.gsfc.nasa.gov/CME_list/halo/) catalog of the Large Angle and Spectrometric Coronagraph (LASCO) on board the *Solar and Heliospheric Observatory* and the CME direction from the Database Of Notifications, Knowledge, Information (DONKI; https://kauai.ccmc.gsfc.nasa.gov/DONKI/); for the two 2017 September CMEs, the space speeds are not available, so the corresponding projected (plane-of-the-sky) velocities are reported. Both flare locations and CME directions are expressed in terms in the heliocentric Earth equatorial (HEEQ) coordinate system.

All of the events are associated with ⩾M-class flares with hard X-ray emission extending above 100 keV (Share et al. 2018) and full halo CMEs in the CDAW catalog. In addition, they were linked to long-duration type II and III radio bursts, indicating the presence of a shock and open field lines, respectively. In particular, the measured type II emission ranges from metric to decameter-hectometric wavelengths for most events (Miteva et al. 2017), suggesting that the shocks accelerating particles formed close to the Sun (Gopalswamy et al. 2017). The heliographic locations of the flares associated with the SEP events listed in Table 1 are shown in Figure 1 for both front- and backside events. The color code indicates the SEP event-integrated intensity above 500 MeV. As expected based on magnetic connectivity considerations, most eruptions populate the western hemisphere; however, eruptions in the eastern hemisphere also contribute to the SEP flux detected near the Earth; in particular, two long-duration high-energy events from near the east limb were observed on 2014 February 25 and September 1.

Figure 2 displays the heliographic distribution of solar events accompanied by LDGRFs registered by *Fermi*/LAT. In particular, the red circles show the locations of eruptions associated with SEP events measured by near-Earth spacecraft (see Table 1), while the blue squares indicate the events for which no significant SEP signal was detected. The latter set, listed in Table 2, essentially corresponds to poorly connected events concentrated in the eastern hemisphere. In particular, columns 9–11 indicate the energy range of SEP observations made by *STEREO-A/B* and near-Earth spacecraft. The high background from a previous event (referred as "bkgr?") may have obscured any SEP signal in the cases of the eruptions on 2011 September 7 and 24, 2012 March 5, and 2013 May 14. In addition, for five events—2011 June 2, 2012 June 3, 2013 May 13, 2013 October 11, and 2013 October 25—*STEREO-B* reported some moderate or large SEP enhancements. However, for the two remaining events on 2012 October 23 and November 27, no SEP signal was observed by *STEREO* and near-Earth spacecraft; above all, these events are peculiar because they were not linked to CMEs. Share et al. (2018) reported an association with magnetic eruptions that may indicate failed CMEs. Nevertheless, such events suggest that the association with fast CMEs is not a necessary requirement for LDGRFs.

For comparison, the green triangles in Figure 2 denote three eruptions without *Fermi*/LAT detections linked to SEP events with a statistically significant proton signal with energies in excess of 500 MeV: the 2012 March 13, 2012 July 8, and 2015 October 29 events. The first two originated close to the western limb and were associated with an M7.9 flare and a full halo CME with a 1884 km s^{-1} space speed and an M6.9 flare and a partial halo CME with a 1497 km s^{-1} projected speed, respectively (Bruno et al. 2018). However, any firm conclusion about attendant >100 MeV γ-ray emission is precluded by the limited exposure of the LAT instrument, which can monitor the Sun for 20–40 contiguous minutes every 1–2 hr depending on the precession of the orbit and the variation of the Sun's latitude (https://hesperia.gsfc.nasa.gov/fermi/lat/lat_solar_exposure_times.txt). To illustrate this point, the time profiles of soft X-ray emission associated with the 2012 March 13 and

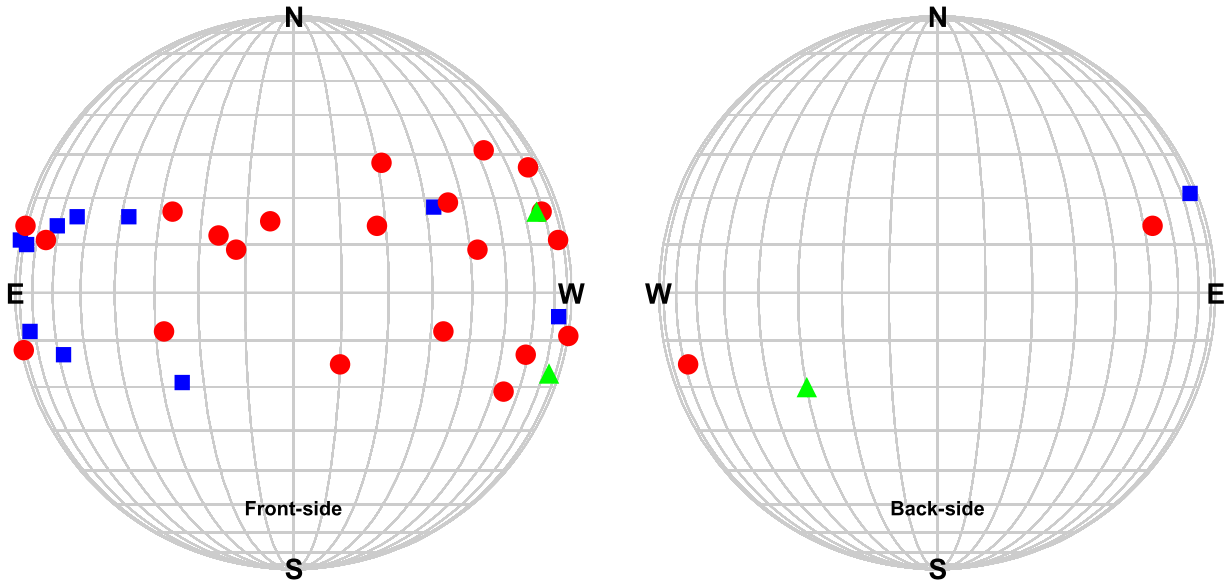

Figure 2. Heliographic distribution of solar flares associated with LDGRFs detected by *Fermi*/LAT and SEPs measured by near-Earth spacecraft. The red circles denote the eruptions linked to both high-energy γ-ray and SEP events (see Table 1), while the blue squares correspond to eruptions with no registered SEP event (see Table 2); for comparison, the green triangles indicate three eruptions associated with SEP events with a statistically significant proton signal above 500 MeV but not linked to >100 MeV γ-ray emission.

2012 July 8 flares are shown in Figure 3. The vertical dashed lines refer to the related CME first appearance times; the horizontal blue lines indicate the average effective area of *Fermi*/LAT, while the hatched regions show the time intervals in which the Sun was occulted in the instrument field of view. Consequently, it can be speculated that *Fermi*/LAT may have missed the detection of relatively short-duration ($\lesssim$1 hr) γ-ray flares. The third eruption producing a >500 MeV SEP event measured by near-Earth spacecraft without *Fermi*/LAT detection occurred on 2015 October 29; however, in this case, it was located well behind the western limb (S20W150). Finally, no LDGRF was detected during the *PAMELA* SEP events with proton energies in excess of 300 MeV but without a statistically appreciable signal above 500 MeV (not shown in Figure 2), such as the events on 2012 July 19, 2013 May 22, and 2014 April 18; these were linked to moderately bright X-ray flares (M7.7-, M5.0-, and M7.3-class, respectively) and, interestingly, fast (1631, 1491, and 1359 km s^{-1} space speed, respectively) halo CMEs (Bruno et al. 2018).

3. Deriving Total Proton Numbers from SEP Events

3.1. Evaluation of the SEP Spatial Distribution

Estimating the total proton number in space from near-Earth measurements of SEP fluxes requires knowledge of the SEP spatial distribution at 1 au and the mean free path during transport. The longitudinal spread of SEPs has generally been attributed to the large spatial extent of the associated CME-driven shock (Mason et al. 1984; Cane et al. 1988) with the earliest estimates inferred from single spacecraft measurements and comparisons with the associated active region (Van Hollebeke et al. 1975; Cane et al. 1986; Reames 1999). However, examples exist of events whose extent is wider than that suggested by the CME shock (e.g., Cliver et al. 1995, 2005), as well as examples of highly prompt intensity increases at widely separated spacecraft (e.g., the 2011 November 3 event; Mewaldt et al. 2013; Richardson et al. 2014). Propagation across the nominal Parker spiral magnetic field is supposed to be enhanced by transport effects in interplanetary space, including cross-field diffusion and early-time nondiffusive propagation in turbulent fields along meandering field lines (see Desai & Giacalone 2016; Laitinen et al. 2018 and references therein). However, the mechanisms that lead to rapid and efficient transport of SEPs within the heliosphere are still not well understood.

Recently, several authors have investigated the SEP spatial distributions by taking advantage of multipoint observations (Lario et al. 2006, 2013; Richardson et al. 2014, 2017; Cohen et al. 2017). These studies show that the SEP peak or event-integrated intensity decreases with increasing longitudinal separation between the solar source and the footpoints of the interplanetary magnetic field (IMF) line connected to the observing spacecraft. With the limited number of observation points available, the longitudinal distribution cannot be determined directly but is usually assumed to be Gaussian. Richardson et al. (2014) obtained an average standard deviation $\sigma = 43°$ for protons between 14 and 25 MeV, consistent with a separate analysis by Lario et al. (2013) for the peak intensity of protons between 25 and 53 MeV. Lario et al. (2006) compared the longitudinal spread of peak and event-integrated intensities and found that their Gaussian standard deviations were not appreciably different. Cohen et al. (2017) performed a fit of event-integrated intensities to periodic Gaussian distributions at two- and three-spacecraft locations and determined an average standard deviation of $43° \pm 1°$ that decreases with increasing energy. Richardson et al. (2017) bracketed the most intense of the nearly 1000 SEP events in their study with a Gaussian standard deviation of $\sigma = 43°$ and suggested that this width is a good indicator of the upper limit of the intensity of 25 MeV proton events as a function of longitude of the solar event with respect to the observer.

In this study, the SEP longitudinal distribution is inferred by combining the event-integrated intensities measured by near-Earth spacecraft (*PAMELA* and *GOES-13/15*) and *STEREO-A/B*.

Table 2
List of LDGRFs Detected by *Fermi*/LAT (Share et al. 2018) without a Clearly Observed Associated SEP Event at Near-Earth Spacecraft

1	2			3				4		
	Flare			CME				SEP Signal		
No.	Onset	Location	Class	1st App.	Speed	Width	Direction	STB	Earth	STA
1	2011 06/02, 07:22	S18E22	C3.7	03/07, 08:12	1147	360	S05E30	$\lesssim$40 MeV	...	...
2	2011 09/07, 22:32	N18W32	X1.8	09/07, 23:06	792	360	N28W40	bkgr?	bkgr?	bkgr?
3[a]	2011/09/24, 09:21	N14E61	X1.9	09/07, 09:48	1936[b]	145	S09E50	>60 MeV	bkgr?	...
4	2012 03/05, 02:30	N16E54	X1.1	03/05, 04:00	1531	360	N22E70	>60 MeV	bkgr?	...
5	2012 06/03, 17:48	N15E38	M3.3	06/03, 18:12	605[b]	180	...	>60 MeV	...	...
6[a]	2012/10/23, 03:13	S15E57	X1.8	...	...	...	...	...	...	...
7	2012 11/27, 15:52	N05W73	M1.6	...	...	...	...	...	...	...
8	2013 05/13, 01:53	N10E89	X1.7	05/13, 02:00	1270	360	N20E94	>60 MeV	...	...
9	2013 05/14, 00:00	N10E89	X3.2	05/14, 01:25	2645	360	N22E90	bkgr?	bkgr?	...
10	2013 10/11, 07:01	N21E103	M4.9	10/11, 07:24	1208	360	S01E106	>60 MeV	...	...
11	2013 10/25, 07:53	S08E73	X1.7	10/25, 08:12	599	360	S02E67	>60 MeV	...	...

Notes. The first column gives the event number. The next three columns report the flare onset (UT), location (degrees), and class based on *GOES* soft X-ray data. Columns 5–8 indicate the associated CME first appearance time (UT), space speed (km s^{-1}), and angular width (degrees) according to the CDAW catalog and direction (degrees) from DONKI. Columns 9–11 display the maximum SEP energy reported by *STEREO-B*, near-Earth spacecraft, and *STEREO-A*, respectively; "bkgr?" indicates that the presence of a high background from a previous event may have obscured any SEP signal enhancement. The dots (...) indicate no data available (missing CME or SEP event).
[a] Impulsive γ-ray emission.
[b] Projected speed (partial halo CMEs).

In the case of *STEREO*, the SEP spectra are evaluated by using the data from the Solar Electron and Proton Telescope (SEPT; 0.084–6.5 MeV, 10 minutes resolution), the Low Energy Telescope (LET; 4–12 MeV, 10 minutes resolution), and the High Energy Telescope (HET; 13.6–100 MeV, 15 minutes resolution), according to the procedure described in Bruno et al. (2019); upper limits on the event-integrated intensities are computed by extrapolating the spectral fits to higher energies. Since *STEREO* measurements are limited to 100 MeV, using the intensities extrapolated to above 500 MeV would result in large uncertainties, producing a significant overestimate of the SEP longitudinal spread. Consequently, we evaluate upper limits for the >500 MeV event-integrated intensity distributions by examining the values obtained for energies higher than 80 MeV (*PAMELA* threshold).

Specifically, we use a periodic Gaussian function with the form

$$G(\delta) = \frac{1}{3}\exp\left(-\frac{\delta^2}{2\sigma^2}\right) + \frac{1}{3}\exp\left(-\frac{\delta_+^2}{2\sigma^2}\right) + \frac{1}{3}\exp\left(-\frac{\delta_-^2}{2\sigma^2}\right), \quad (1)$$

with δ given by the great-circle or orthodromic distance from the peak of the SEP spatial distribution (β_{sep}, α_{sep}),

$$\delta = \arccos[\sin(\alpha)\sin(\alpha_{sep}) + \cos(\alpha)\cos(\alpha_{sep})\cos(\beta - \beta_{sep})], \quad (2)$$

where β and α are the HEEQ longitude and latitude, σ is the distribution standard deviation, and the terms associated with

$$\delta_\pm = \arccos[\sin(\alpha)\sin(\alpha_{sep}) + \cos(\alpha)\cos(\alpha_{sep})\cos(\beta - \beta_{sep} \pm 2\pi)] \quad (3)$$

account for the possible contribution from particles propagating at angles >180° from the center of the distribution, ensuring that $G(\delta) = G(\delta \pm 2\pi)$ (Cohen et al. 2017). The use of a periodic function is important, especially for SEP events characterized by a broad longitudinal distribution. In previous studies, the latitudinal magnetic connectivity to the SEP sources (Dalla & Agueda 2010; Gopalswamy & Mäkelä 2014) was typically neglected compared to longitudinal variations, and the inclination of the propagation axis was ignored when fitting spatial distributions. However, we note that, unless α_{sep} is null, the function describing the distribution projection on the *X*–*Y* plane is not Gaussian but includes a factor depending on α_{sep},

$$G(\beta) = \frac{1}{3}\exp\left\{-\frac{\arccos^2[\cos(\alpha_{sep})\cos(\beta - \beta_{sep})]}{2\sigma^2}\right\} + ..., \quad (4)$$

where the two terms centered at $\beta_{sep} \pm 2\pi$ are omitted for brevity. Consequently, fitting the particle intensities measured by spacecraft at 1 au with a Gaussian function will result in a systematically larger standard deviation for higher-latitude events; in particular, for 2012 January 23 and 27, we estimate an ~3° (~8%) difference. To a first approximation, α_{sep} is assumed to coincide with the latitudinal angle α_{flare} describing the parent flare location (see column 7 in Table 1).

Particle transport through the IMF is accounted for by computing the footpoints of the Parker spiral field lines crossed by the spacecraft, which are mapped ballistically back to 30 R_s and down to the photosphere based on measured plasma speed data by using the Predictive Science web tools (http://www.predsci.com/stereo/spacecraft_mapping.php and http://www.predsci.com/hmi/spacecraft_mapping.php); as results are available with a 1 hr resolution, the calculation is performed for the hour before the flare onset. However, we do not use magnetic footpoints at the photosphere for the estimate of N_{SEP} because the results would be model-dependent (see, e.g., Lario et al. 2017). Consistent with Cohen et al. (2017), the

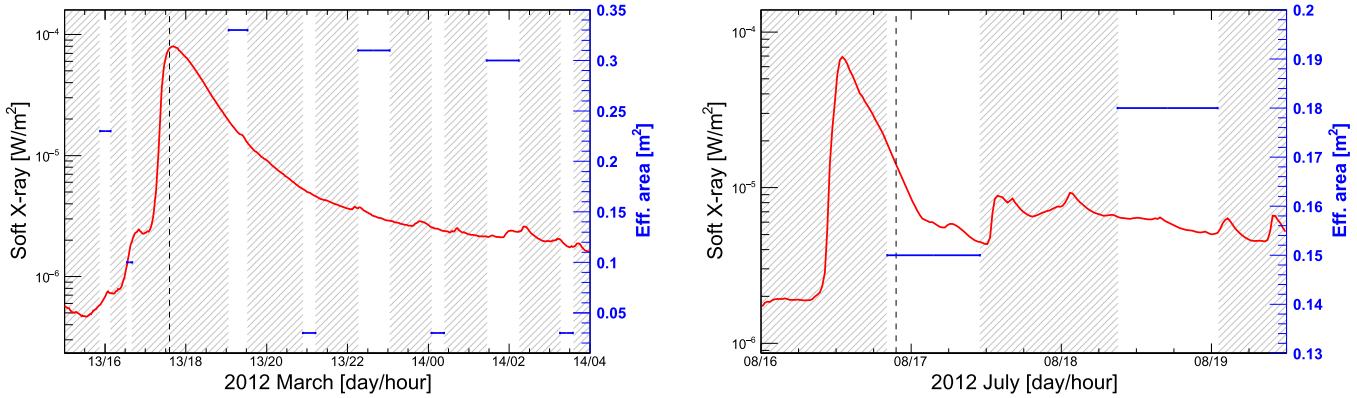

Figure 3. Time profiles of soft X-ray emission during the 2012 March 13 and 2012 July 8 eruptions. The vertical dashed lines refer to the related CME first appearance times in the LASCO C2 coronagraph. The horizontal blue lines indicate the average effective area of *Fermi*/LAT, while the hatched regions show the time intervals in which the Sun was occulted in the instrument field of view.

differences between footpoints obtained at 30 R_s and at the photosphere are of the order of $\sim 10^{\circ}$, which can be assumed as an indication of the associated uncertainty. On the other hand, significantly larger deviations are found for the 2014 February 25 event, for which the derived *STEREO-A/B* footpoints at the photosphere are very close (see Figure 18 in Cohen et al. 2017), in contrast to the large discrepancy in terms of detected particle intensities. Because the footpoints of the field lines connecting the spacecraft generally do not lie in the *X*–*Y* plane, and in order to apply Equation (4) to the measured intensities, we apply a correction factor to account for the spacecraft footpoint latitude $\alpha_{\rm sc}$,

$$K_{\alpha} = \exp\left(\frac{\delta_{\rm sc}^2 - \delta_{\rm sc,0}^2}{2\sigma^2}\right), \quad (5)$$

where $\delta_{\rm sc}$ and $\delta_{\rm sc,0}$ are the great-circle distances from the peak of the SEP spatial distribution evaluated with respect to the spacecraft footpoints and their projection on the *X*–*Y* plane ($\alpha_{\rm sc} = 0$), respectively. Since σ is unknown a priori, we perform an iterative procedure until the fit results become stable. We note that, even though $\alpha_{\rm sc}$ is typically a few degrees, the differences in terms of great-circle distances are much larger, and thus the associated correction can be significant. Finally, the small discrepancies (<5%) regarding radial distances are neglected, and all of the spacecraft are assumed to be located exactly at 1 au.

3.2. Estimate of Transport Effects in Interplanetary Space

The transport of SEPs in the interplanetary medium is governed not only by the large-scale magnetic field geometry but also by small-scale scattering from turbulence. One consequence is that particles may pass the distance of the observing spacecraft several times (Zank et al. 2006), requiring a correction of the flux and, in turn, the local number density. Zank et al. (2006) modeled the number of crossings at 1 au, $N_{\rm cross}(E)$, for SEPs accelerated by both weak and strong shocks and found an $\overline{N}_{\rm cross} \sim 2$–4 mean value above 100 MeV, but, on occasion, high-energy particles experience multiple crossings as high as 15. Chollet et al. (2010) used numerical simulations of particle transport to determine $\overline{N}_{\rm cross} \sim 6$–7 for 100 MeV.

Since SEP intensity and anisotropy distributions depend on the scattering mean free path λ parallel to the magnetic field (Palmer 1982), we estimate $\overline{N}_{\rm cross}$ by means of simulations of relativistic proton propagation under a variety of scattering conditions. We consider two separate test particle simulation codes, the first (simulation code 1 (SC1)) presented by Chollet et al. (2010) and the second (simulation code 2 (SC2)) by Battarbee et al. (2018). For both codes, we assumed an impulsive injection of monoenergetic isotropic particles at 0.1 au and followed them for 10 days, including magnetic focusing and scattering off an unspecified plasma turbulence field. Particle crossings over the entire 1 au sphere are added together and averaged over the monoenergetic population considered.

Table 3
Average Number of 1 au Crossings at Sample Proton Energies as Predicted by SC1 (Chollet et al. 2010) for Different Turbulence Models

Energy	Turbulence Model 1		Turbulence Model 2	
(MeV)	λ = const., $\lambda_0 = 0.1$ au	λ = const., $\lambda_0 = 0.5$ au	$\lambda \propto r_g$, $\lambda_0 = 0.1$ au	$\lambda \propto r_g$, $\lambda_0 = 0.5$ au
500	18.4	7.0	14.5	4.7
1000	16.5	5.9	11.8	4.1
2000	17.2	5.0	10.6	3.6

Using SC1, we let the turbulence take one of two forms: either uniform from the launch radius to 1 au (turbulence model 1) or varying in proportion to the gyrocyclotron radius r_g (turbulence model 2). The resulting transport calculations predict the time-dependent development and decay of the intensity at 1 au. The mean numbers of crossings as a function of energy are reported in Table 3 for both turbulence models. A flat heliospheric current sheet (HCS) is assumed, and the results are valid for a positive solar magnetic field polarity in the northern hemisphere. It should be noted that $\overline{N}_{\rm cross}$ distributions are very broad, as the associated rms values (not shown in the table) are of the same magnitude as the mean values.

The average number of 1 au crossings was also calculated by means of SC2 (Battarbee et al. 2018; Marsh et al. 2013), a code that can include the effects of a wavy HCS. We use λ = const. (turbulence model 1) for these simulations. Table 4 shows how the number of crossings varies for different configurations of the HCS, including no, flat, or wavy HCS. Using the standard galactic cosmic-ray definition, A^+ refers to a situation in which the polarity of the IMF is positive (outward) in the northern hemisphere and negative (inward) in the southern hemisphere, with the opposite for A^-. The number of crossings for $E = 1000$ MeV, $\lambda_0 = 0.1$ au, flat HCS, and A^+ compares well

Table 4
Average Number of 1 au Crossings at Sample Proton Energies as Predicted by SC2 (Battarbee et al. 2018) for Different Types of HCS Configurations, Mean Free Path Values, and Solar Magnetic Polarities

Energy (MeV)	λ_0 (au)	HCS Configuration	Magnetic Polarity	$\overline{N}_{\rm cross}$
1000	0.1	No HCS	+ both poles	31
1000	0.1	No HCS	− both poles	28
500	0.1	Flat HCS	A^+	19
500	0.1	Flat HCS	A^-	29
500	0.5	Flat HCS	A^+	8
500	0.5	Flat HCS	A^-	11
1000	0.1	Flat HCS	A^+	15
1000	0.1	Flat HCS	A^-	28
500	0.1	Wavy HCS	A^+	21
500	0.1	Wavy HCS	A^-	30
500	0.5	Wavy HCS	A^+	8
500	0.5	Wavy HCS	A^-	11
1000	0.1	Wavy HCS	A^+	17
1000	0.1	Wavy HCS	A^-	29
1000	0.5	Wavy HCS	A^+	7
1000	0.5	Wavy HCS	A^-	11

Note. Here A^+ corresponds to a positive polarity north pole and negative polarity south pole, while the opposite holds for A^-; "+/− both poles" denote a positive/negative polarity for both poles.

with that of SC1, as shown in Table 3 (corresponding to a run with flat HCS and A^+), showing that the two codes are in good agreement. Table 4 shows that at particle energies of 1 GeV, there is a large difference in the number of crossings for the A^+ and A^- cases. The difference is similar for the cases of both flat and wavy HCS. The cause of this difference is the particle drift along the HCS, which for the A^+ case helps to move protons outward from the inner heliosphere faster. A full simulation of the 2012 May 17 event, with the initial proton distribution given by a power law, shows good agreement between the SC2 and *PAMELA* intensity time profiles when $\lambda_0 = 0.3$ au (S. Dalla et al. 2019, in preparation).

The solar polarity reversal during cycle 24 was unusually complex. In fact, based on the measurements of the Wilcox Solar Observatory, the northern polar field changed polarity in 2012 June, while the southern polar field reversed in 2013 July; however, additional analyses of solar data suggest that the field reversal was completed in 2014–2015 (see, e.g., Janardhan et al. 2018 and references therein).

Figure 4 shows decay times deduced from the time-intensity profiles for the SEPs observed by *PAMELA*. With the exception of the two eastern events on 2014 February 25 and 2014 September 1, for which we expect significant cross-field diffusion, the decay times all show similar energy dependence. Table 5 gives the values of the decay times from SC1 for the two turbulence models considered. As expected from diffusive transport theory, a shorter mean free path results in a longer decay time. The SC1 values that best match the *PAMELA* observations are those for turbulence model 1 (λ = constant), with a mean free path at 1 au of $\lambda_0 = 0.1$ au. The simulation results are in better agreement with the predictions of model 1 for λ = constant. In particular, the analysis of the 2012 May 17 event suggests a value of ∼0.3 au for the mean free path. For the purpose of this work, because we compute upper limits on the number of SEPs at 1 au (see below), we conservatively assume $\lambda_0 = 0.5$ au, and we use the number of crossings estimated at 500 MeV with the wavy HCS configuration and A^-/A^+ magnetic polarity for SEP events occurring before/after 2012 June, respectively (see Table 4). Finally, we note that model calculations do not include possible effects related to local solar wind structures, including magnetic mirroring from nearby reflecting boundaries (see, e.g., Tan et al. 2009).

3.3. Assessment of the Number of SEP Protons at 1 au

After estimating the SEP spatial distribution at 1 au and the mean free path during transport, we can derive the total number of solar protons above 500 MeV using the following relation:

$$N_{\rm SEP} = \overline{N}_{\rm cross}^{-1} \int_{4\pi} d\Omega \int_S dS(\boldsymbol{J}\cdot\boldsymbol{n}) \tag{6}$$

$$= \overline{N}_{\rm cross}^{-1} \int_{4\pi} d\Omega \int_S dS \cos(\theta)\, J(\Omega, S), \tag{7}$$

where S is the heliocentric spherical surface with radius $R_o = 1$ au, $d\Omega = d\phi\, d\theta \sin(\theta)$ is the solid-angle element with polar angles ϕ and θ defining the particle velocity direction in the reference frame centered at a point on the sphere, and $J = J(\Omega, S)$ is the event-integrated intensity for energies >500 MeV; the dot product accounts for the fact that the flux at an angle θ with respect to the local normal to the sphere surface (n is the unit vector) is proportional to $\cos(\theta)$. Consequently, for an isotropic flux, $J(\Omega, S) = J(S)$ (independent on Ω), the integration over the 4π detection solid angle subtended at a point on the sphere gives

$$\int_{4\pi} d\Omega \cos(\theta)\, J(\Omega, S) = \int_0^{2\pi} d\phi \int_0^{\pi} d\theta \sin(\theta)\cos(\theta)\, J(\phi, \theta, S) = 2\pi J(S). \tag{8}$$

Integrating Equation (8) over the whole spherical surface and assuming a Gaussian spatial distribution $J(S) = J_{\rm max} G(\delta)$, where the amplitude $J_{\rm max}$ is the maximum particle intensity at 1 au (corresponding to the SEP propagation axis) and $G(\delta)$ is given by Equation (1), Equation (6) reduces to

$$N_{\rm SEP} = 2\pi\, \overline{N}_{\rm cross}^{-1}\, J_{\rm max} \int_S dS\, G(\delta) \tag{9}$$

$$= 2\pi\, \overline{N}_{\rm cross}^{-1}\, J_E\, S_J\, C_{\rm spa}, \tag{10}$$

where J_E is the >500 MeV event-integrated intensity measured by *PAMELA* and S_J is the spherical area weighted by the particle spatial distribution,

$$S_J = 2\pi R_o^2 \int_0^{\pi} d\delta\, \sin\delta\, G(\delta), \tag{11}$$

where δ is the great-circle distance with respect to the peak of the SEP spatial distribution (Equation (2)). The Gaussian standard deviation is derived by fitting the longitudinal distribution given by >80 MeV particle intensities measured by *STEREO* and *PAMELA* by means of the function given by Equation (4). The integration of Equation (11) is then performed by means of numerical techniques. Finally, $C_{\rm spa}$ accounts for the fact that, in general, *PAMELA*'s observations are not made on IMF lines that connect with the peak of the

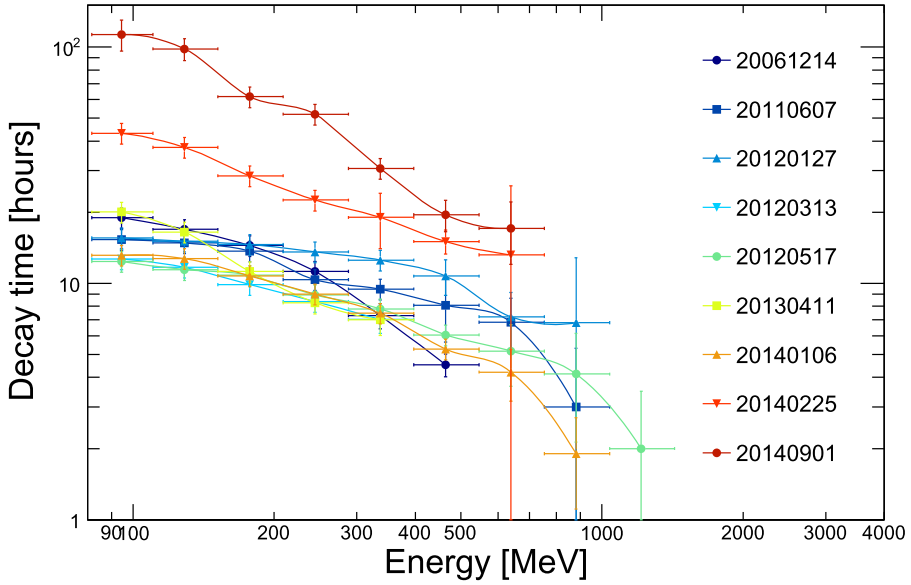

Figure 4. Decay times of proton intensities as a function of energy for sample SEP events measured by *PAMELA*. The curves are to guide the eye.

Table 5
Decay Times for 1 au Intensity Time Profiles at Sample Proton Energies Predicted by SC1 (Chollet et al. 2010) for Different Turbulence Models

	Turbulence Model 1		Turbulence Model 2	
Energy (MeV)	λ = const., $\lambda_0 = 0.1$ au τ (hr)	λ = const., $\lambda_0 = 0.5$ au τ (hr)	$\lambda \propto r_g$, $\lambda_0 = 0.1$ au τ (hr)	$\lambda \propto r_g$, $\lambda_0 = 0.5$ au τ (hr)
100	>15.5	2.8	10.6	1.5
200	13.1	2.1	8.7	1.3
500	6.5	1.5	5.7	1.1
1000	4.8	1.4	3.7	1.0
2000	2.6	1.1	2.6	1.0

particle distribution,

$$C_{\rm spa} = \exp\left(\frac{\delta_{pam}^2}{2\sigma^2}\right), \quad (12)$$

where δ_{pam} is the great-circle distance between *PAMELA*'s magnetic footpoints and the peak of the SEP spatial distribution, so that

$$J_{\rm max} = J_E\, C_{\rm spa}. \quad (13)$$

As a final remark, we note that the mathematical formulation described in this section provides a significantly more robust basis to our calculation, representing a major improvement with respect to the simpler approaches adopted in previous studies.

4. Results

4.1. SEP Spatial Distributions

The numbers of protons $N_{\rm SEP}$ and $N_{\rm LDGRF}$ were derived for the SEP events in common with the "light-bucket" analysis by Share et al. (2018; see Table 1), with the exception of the 2013 May 13 event, for which no appreciable >500 MeV SEP signal was measured by near-Earth spacecraft; the 2013 May 15 eruption, due to the high background from a previous event that may have obscured any clear SEP enhancement in the measurements of *STEREO-B*, the best-connected spacecraft; and the 2015 June 21 event, occurring after the loss of communications with *STEREO-B* in 2014 October. The selected sample consists of 14 events mostly located in the visible western hemisphere, but it also includes poorly connected events such as the 2014 February 25 eastern limb and 2014 September 1 backside events. The *PAMELA* and *STEREO-A/B* event-integrated intensities are displayed in Figure 5 as a function of the longitudinal difference $\Delta\beta = \beta_{\rm sc} - \beta_{\rm sep}$ (connection angle) between the spacecraft magnetic footpoints at 30 R_s and the location of the parent flare; thus, positive (negative) angles correspond to footpoints west (east) of the flare.

The SEP distributions are influenced by several factors. For the 2011 June 7 event, the intensities measured by *STEREO-A/B* are dominated by the background from a previous event. Here we assume a standard deviation of 40.4°, which, as discussed below, represents the mean σ that characterizes the connection-angle dependence of the event-integrated >80 MeV intensity spectra measured by *PAMELA*. The same standard deviation is assumed for the 2012 July 7 event, for which no significant SEP signal was measured by *STEREO-B*; the integration interval used for the intensities measured by *PAMELA* and *STEREO-A* is limited by the onset of a following SEP event on July 8, resulting in intensities that are underestimated. Similarly, the time integration over the 2012 January 23 event is limited by the onset of the January 27 event, and the intensities measured during the latter include a component from the previous event. In the case of the 2014 September 1 event, large gaps present in the *STEREO-A* data preclude constructing event-integrated intensities; based on the comparison of the respective time profiles, the SEP flux is assumed to be equal to the one measured by *STEREO-B*. The time-integrated intensities measured during the 2011 March 7 event include particles injected at three different eruptions. In particular, those registered by *STEREO-B* comprise a significant component from the previous well-connected eruption, originating a few hours before. This translates to a longitudinal distribution that is narrower with a peak closer to the Earth's magnetic footpoints. Similarly, SEP intensities measured by

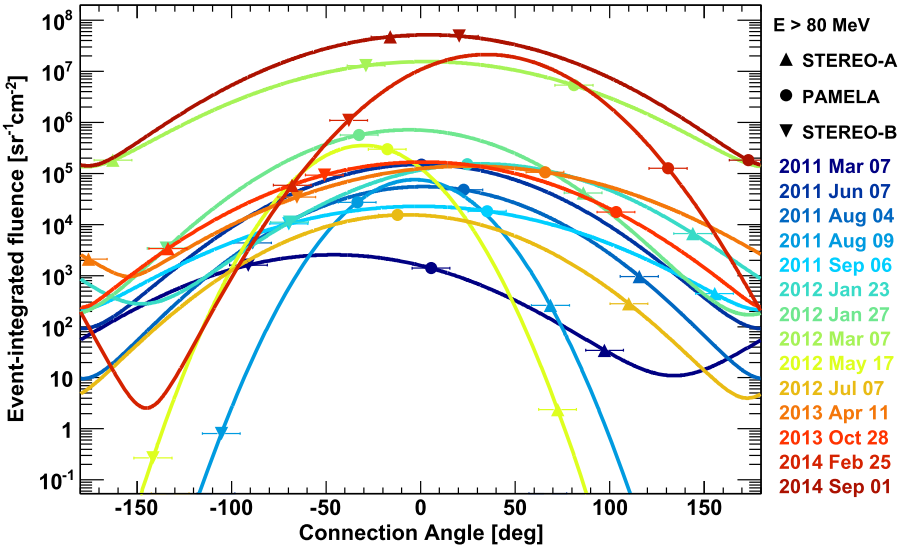

Figure 5. Longitudinal extent of SEP events determined from the fits (Equation (4)) of the event-integrated intensities (>80 MeV) measured by *PAMELA* and *STEREO-A/B* as a function of the longitudinal difference (connection angle) between the spacecraft magnetic footpoints at 30 R_s and the location of the parent flare.

STEREO-B and, to a lesser extent, also by *STEREO-A* during the 2013 October 28 event include a contribution from another eruption occurring 3 days before, resulting in an overestimate of the total number of protons $N_{\rm SEP}$ at 1 au.

Some studies reported that the centers of the derived SEP distributions tend to lie west of the flare location (Lario et al. 2006, 2013; Cohen et al. 2017), although this trend was not confirmed by other analyses (e.g., Richardson et al. 2014). Lario et al. (2014) suggested that this displacement would be likely due to the fact that the maximum peak intensity is observed at some helioradial distance for which the eruption occurs eastward with respect to the footpoints of the nominal field line connecting the spacecraft with the Sun. The effect is expected to be larger at lower energies as particles escape from the acceleration region at higher heights (Cohen et al. 2017). The SEP event sample analyzed in this work is characterized by significant variability, with eight (six) event distributions centered at positive (negative) connection angles $\Delta\beta$, resulting in an $\sim$0.7° mean angle between the flare and the peak of the SEP distribution and an $\sim$22° rms value. In addition, effects related to the multiple injections discussed above are also likely to contribute. A majority of the SEP events with intensities reaching 1 GeV are confined to a narrow swath of longitudes, suggesting that the longitudinal spread at higher energies is even narrower than at 80 MeV, consistent with the energy dependence reported by Cohen et al. (2017) below 10 MeV. Thus, the longitudinal distribution inferred from >80 MeV protons is an upper bound to the longitudinal extent at higher energies. This upper limit is also justified by the fact that we assume the same angular distribution for the latitudinal extent as the longitudinal dependence (i.e., $\sigma = \sigma_\alpha = \sigma_\beta$). The normalized SEP spatial distributions $G(\delta) = G(\beta,\ \alpha)$ (Equation (1)) are shown in Figure 6 as a function of HEEQ coordinates. The stars show the parent flare locations, the circles indicate *PAMELA*'s magnetic footpoints, and the upward- and downward-pointing triangles show those of *STEREO-A* and *-B*, respectively. Only SEP events with three spacecraft measurements are displayed. The angles defining the direction of the peak of the SEP spatial distribution are reported at the top of the panels.

The results of the calculation of the SEP parameters at 1 au are shown in Table 6. The first two columns give the SEP event number and date. Columns 3–13 list the longitudinal and latitudinal connection angles between the flare location and the spacecraft magnetic footpoints at 30 R_s and the event-integrated intensities measured by the three spacecraft above 80 MeV. For *STEREO-A/B*, upper limits are provided, and the spacecraft location is also given; "bkgr" indicates that a high background from a previous event may have obscured any SEP signal. Columns 14–15 display the Gaussian fit parameters (peak longitude and standard deviation), while the values of the weighted spherical surface S_J and the spatial correction factor $C_{\rm spa}$ (see Equations (11) and (12)) are reported in columns 16 and 17. Column 18 gives the number of crossings used for the calculation. Column 19 lists the numbers of SEP protons above 500 MeV at 1 au. For comparison, the numbers of protons interacting at the Sun inferred from *Fermi*/LAT observations by Share et al. (2018) are shown in column 20; they include the correction factor accounting for a downward isotropic angular distribution (see Table 3 in Share et al. 2018).

The average σ value estimated for the analyzed SEP event sample is $\sim$41°, characterized by a large rms value ($\sim$11°). For two SEP events, the one on 2011 August 9 and the GLE event on 2012 May 17, the standard deviation is small ($\sim$21°), resulting in a narrow distribution that peaks close to the Earth's magnetic footpoints. On the other hand, the three events on 2011 September 6, 2013 April 11, and 2014 September 1 are very broad, with a σ value larger than 50°; however, as aforementioned, the integrated intensities measured during the 2011 September 6 event by *PAMELA* and *STEREO-A* include a component from the previous SEP event, probably resulting in an overestimate of the spatial extent. For the other two events, it can be speculated that the broad distributions are due to significant transport effects, such as cross-field diffusion and IMF corotation in combination with the extended SEP source provided by the CME-driven shock. The rest of the SEP sample is characterized by a standard deviation between 30° and 50°.

Three of the considered events, the 2012 January 23 and 27 events and the 2014 February 25 event, were also investigated by Cohen et al. (2017) at much lower energies ($\leqslant$10 MeV). In general, the standard deviation of the spatial distribution is

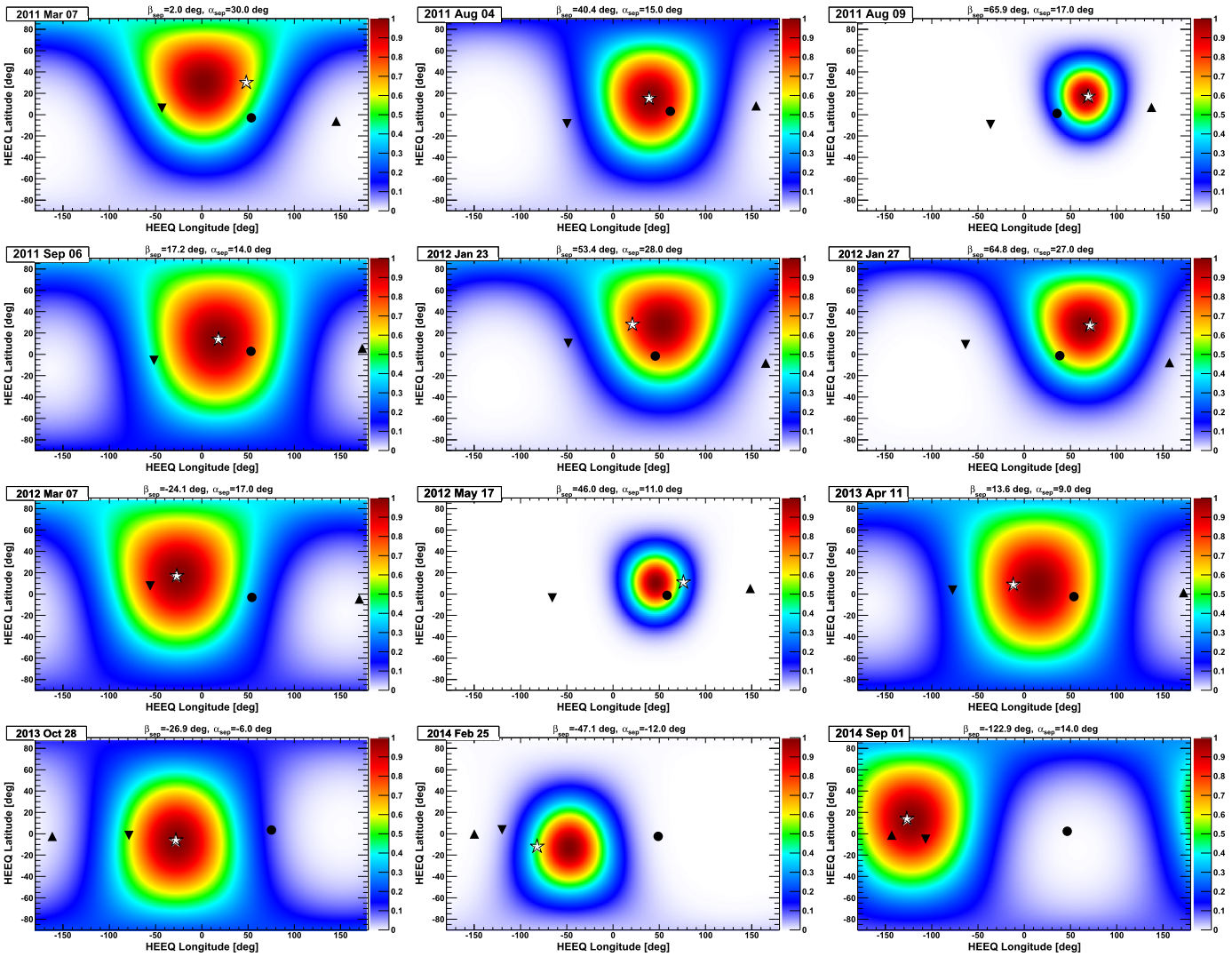

Figure 6. Normalized SEP spatial distributions in HEEQ coordinates $G(\delta) = G(\beta,\ \alpha)$ (Equation (1)) inferred by the >80 MeV event-integrated intensity measurements. The stars show the parent flare locations, the circles indicate *PAMELA*'s magnetic footpoints, and the upward- and downward-pointing triangles refer to those of *STEREO-A* and *-B*, respectively; only SEP events with three spacecraft measurements are displayed. The direction of the peak of the SEP spatial distribution is reported at the top of the panels.

expected to decrease with increasing energy as a consequence of several acceleration and/or transport related phenomena. This can reasonably explain the relatively small differences regarding the 2014 February event, for which the derived standard deviations are consistent (33° at 10 MeV versus 30° above 80 MeV). On the other hand, they found significantly larger σ values for the 2012 January 23 and 27 events (respectively, 45° and 49° at 10 MeV versus 42° and 37° above 80 MeV). As discussed in Section 3, projection effects have a significant impact for high-latitude events such as those in 2012 January, and the use of a Gaussian function to fit the particle intensities neglecting the latitude of the SEP propagation axis results in some overestimate of the distribution standard deviation. The correction given by Equation (4) likely constitutes a major source of discrepancy between the two calculations.

4.2. Comparison between N_{LDGRF} and N_{SEP}

The comparison between proton numbers derived from the >100 MeV γ-ray emission ($N_{\rm LDGRF}$) and SEPs at 1 au ($N_{\rm SEP}$) is displayed in Figure 7. The solid and dashed lines mark the 1-to-1 and 1-to-100 correspondences, respectively. The *Fermi*/LAT proton numbers are from Share et al. (2018) and corrected for anisotropic effects characterized by the downward proton distribution (Mandzhavidze & Ramaty 1992). The vertical error bars include the uncertainties on LDGRF proton numbers from Share et al. (2018). For the quantity $N_{\rm SEP}$, upper limits are provided accounting for the assumptions made in the spatial distribution estimate, as discussed earlier. A large scatter among the points can be observed, with no significant correlation, as confirmed by the low values of the Kendall's τ and Spearman rank correlation coefficients, reported on the plot along with the corresponding p-values (significance level). The $N_{\rm SEP}/N_{\rm LDGRF}$ ratio spans more than 5 orders of magnitude, ranging from $\sim 7.8 \times 10^{-4}$ to $\sim 5.0 \times 10^{2}$, with a mean value of $\sim$78.

The lowest ratio values are obtained for the 2011 March 7 and 2012 January 23 SEP events, which were characterized by very soft energy spectra in both *PAMELA* and *STEREO* observations. Gopalswamy et al. (2018) suggested that the relatively low SEP intensities measured during the 2011 March

Table 6
SEP Longitudinal Extent at 1 au

1		2				3			4				5		6	7	8	9	10
SEP Event		*STEREO-B*				*PAMELA*			*STEREO-A*				Fit Param.		S_J	C_{spa}	$\overline{N}_{cross}$	N_{SEP}	N_{LDGRF}
No.	Date	Loc.	$\Delta\beta$	$\Delta\alpha$	Intensity	$\Delta\beta$	$\Delta\alpha$	Intensity	Loc.	$\Delta\beta$	$\Delta\alpha$	Intensity	β_{sep}	σ					
1	2011 Mar 7	−93.9	−91.0	−23.8	1.6×10^{3}[a]	5.6	−33.0	1.4×10^{3}[b]	88.7	97.3	−36.1	3.5×10^{1}	2.0	44.5	6.97×10^{26}	2.42	11	1.18×10^{26}	$(1.51 \pm 0.44) \times 10^{29}$
2	2011 Jun 7	−91.9	−108.2	13.8	bkgr	0.5	21.0	1.5×10^{5}	96.0	67.4	28.2	bkgr	54.5	41.0	6.08×10^{26}	1.14	11	1.93×10^{29}	$(2.20 \pm 0.80) \times 10^{28}$
3	2011 Aug 4	−91.9	−88.8	−23.5	4.4×10^{3}	22.9	−11.9	4.8×10^{4}	101.3	115.7	−6.8	9.6×10^{2}	40.4	39.5	5.72×10^{26}	1.21	11	5.04×10^{27}	$(2.52 \pm 0.63) \times 10^{28}$
4	2011 Aug 9	−92.0	−105.4	−26.2	8.1×10^{-1}	−33.5	−15.8	2.7×10^{4}	101.8	68.7	−10.1	2.6×10^{2}	65.9	21.0	1.80×10^{26}	3.69	11	1.41×10^{28}	$(5.60 \pm 1.40) \times 10^{27}$
5	2011 Sep 6	−94.0	−69.7	−19.7	1.0×10^{4}	35.2	−11.1	1.8×10^{4}[a]	103.9	155.5	−8.3	4.4×10^{2}[a]	17.2	54.2	9.42×10^{26}	1.27	11	7.09×10^{28}	$(5.06 \pm 0.92) \times 10^{28}$
6	2012 Jan 23	−113.0	−69.3	−17.7	1.1×10^{4}[c]	24.7	−29.6	1.5×10^{5}[c]	108.8	144.0	−36.1	6.7×10^{3}[c]	53.4	42.0	6.35×10^{26}	1.30	11	2.89×10^{27}	$(6.60 \pm 1.32) \times 10^{28}$
7	2012 Jan 27	−113.6	−134.5	−17.9	3.4×10^{3}[a]	−32.5	−28.2	5.6×10^{5}[a]	108.9	86.0	−34.7	4.2×10^{4}[a]	64.8	36.9	5.09×10^{26}	1.70	11	9.74×10^{29}	$(1.87 \pm 1.10) \times 10^{28}$
8	2012 Mar 7	−116.7	−28.9	−9.4	1.3×10^{7}	81.1	−20.0	5.3×10^{6}	110.6	−162.7	−21.6	1.8×10^{5}	−24.1	52.6	9.03×10^{26}	3.14	11	1.75×10^{31}	$(3.81 \pm 0.68) \times 10^{30}$
9	2012 May 17	−116.8	−141.6	−14.7	2.7×10^{-1}	−17.6	−12.2	3.0×10^{5}	116.0	72.5	−5.8	2.4×10^{0}	46.0	20.8	1.78×10^{26}	1.41	11	7.56×10^{29}	$(2.10 \pm 1.40) \times 10^{27}$
10	2012 Jul 7	−114.5	−132.5	4.7	bkgr	−12.3	14.0	1.5×10^{4}[c]	120.7	110.2	20.0	2.8×10^{2}[c]	51.8	41.0	6.08×10^{26}	1.07	8	7.10×10^{27}	$(1.89 \pm 0.63) \times 10^{28}$
11	2013 Apr 11	−140.7	−65.4	−5.4	3.4×10^{4}	65.8	−11.5	1.1×10^{5}	134.8	−175.7	−7.7	2.1×10^{3}	13.6	54.1	9.41×10^{26}	1.35	8	8.47×10^{28}	$(1.70 \pm 0.69) \times 10^{28}$
12	2013 Oct 28	−141.2	−50.8	4.5	9.3×10^{4}	103.3	9.6	1.8×10^{4}	149.5	−133.6	3.7	3.4×10^{3}[a]	−26.9	48.1	7.87×10^{26}	9.73	8	4.41×10^{29}	$(8.80 \pm 4.40) \times 10^{26}$
13	2014 Feb 25	−159.3	−38.0	15.7	1.1×10^{6}	130.9	9.5	1.3×10^{5}	153.7	−67.9	11.8	5.9×10^{4}	−47.1	29.7	3.45×10^{26}	174.24	8	3.77×10^{31}	$(1.14 \pm 0.52) \times 10^{30}$
14	2014 Sep 1	−159.8	20.5	−19.2	4.9×10^{7}	173.4	−11.7	1.8×10^{5}	167.8	−16.2	−15.1	4.7×10^{7}	−122.9	48.1	7.89×10^{26}	261.00	8	2.35×10^{32}	$(1.99 \pm 0.90) \times 10^{30}$

Notes. The first two columns report the SEP event number and date. Columns 3–13 give the HEEQ longitude (degrees) of the *STEREO-A/B* location ("Loc."), the longitudinal ($\Delta\beta$, degrees) and latitudinal ($\Delta\alpha$, degrees) deviation between the footpoints of *PAMELA* or *STEREO-A/B* at 30 R_s, and the parent flare location, along with the event-integrated intensities (sr^{-1} cm^{-2}) above 80 MeV measured by the three spacecraft. Upper limits are provided for the *STEREO*s; "bkgr" indicates that a high background from a previous event may have obscured any SEP signal. Columns 14–17 indicate the peak longitude β_{sep} (degrees) and standard deviation σ (degrees) of the SEP spatial distribution derived from the fit of measured intensities (Equation (4)), the weighted surface (cm^2), and the spatial correction factor defined by Equations (11) and (12). Column 18 gives the number of crossings used for the calculation. Finally, columns 19–20 report the total number of SEP protons above 500 MeV at 1 au and the number of protons interacting at the Sun inferred from *Fermi*/LAT observations by Share et al. (2018).

[a] Component from a previous SEP event.

[b] Upper limit.

[c] Integration interval limited by the onset of a successive SEP event.

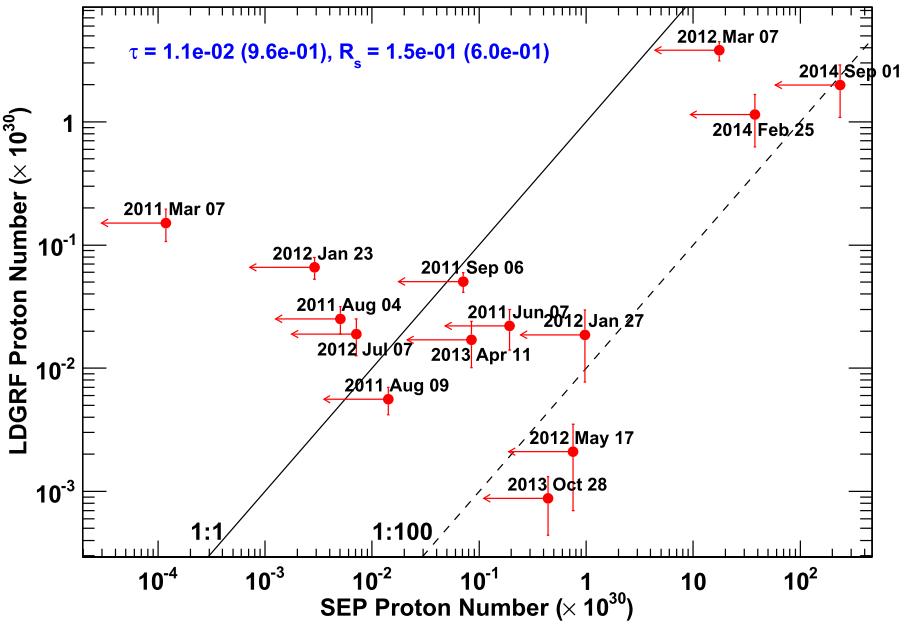

Figure 7. Number of protons deduced from *Fermi*/LAT (Share et al. 2018) compared with the number of protons determined from *PAMELA* and *STEREO-A/B*. The solid and dashed lines mark the 1-to-1 and 1-to-100 correspondences, respectively. The Kendall's τ and Spearman rank (R_s) correlation coefficients are also reported, along with the corresponding p-values.

7 event are probably due to the poor latitudinal magnetic connectivity. As our calculation accounts for these effects by means of the spatial factor given by Equation (12), we conclude that the very low $N_{\rm SEP}/N_{\rm LDGRF}$ ratio cannot be explained by connectivity arguments. Indeed, the ∼33° latitudinal deviation between the *PAMELA* magnetic footpoints and the flare location for this event is, for instance, comparable to the corresponding angle for the 2012 January 27 event (∼28°; see Table 6), which, however, extended above 500 MeV. An alternative explanation for the soft spectra is provided by the values of the shock formation height, a key factor in determining the maximum energy of SEPs, as the acceleration efficiency strongly depends on the coronal magnetic field strength, which decreases with increasing heliocentric distance (Zank et al. 2000). Most events shown in Figure 7 were accompanied by type II radio bursts with high (>100 MHz) starting frequencies (see, e.g., Miteva et al. 2017), suggesting high local plasma densities and thus small (<1.6 R_s) shock formation heights based on the empirical formula by Gopalswamy et al. (2013). In contrast, using *STEREO* coronagraphic and EUV observations close to the solar surface, Gopalswamy et al. (2013) estimated a 1.93 R_s height for the 2011 March 7 event, whose type II emission was limited to relatively lower frequencies ($f_{\rm max}$ ∼ 50 MHz). A similar height (2 R_s) was computed by Joshi et al. (2013) for the 2012 January 23 event; they also proposed that the unusually high $f_{\rm max}$ value (∼200 MHz) associated with the eruption was probably due to the fact that the shock formed in the body of a previous CME.

The highest $N_{\rm SEP}/N_{\rm LDGRF}$ ratio values correspond to the 2012 May 17 GLE event and the 2013 October 28 event, for which the detected >100 MeV γ-ray emission was rather low. The $N_{\rm SEP}$ is somewhat overestimated for the latter event due to the presence of a previous event, but this alone is insufficient to account for the high $N_{\rm SEP}/N_{\rm LDGRF}$ ratio. Similar circumstances in other events also do not produce the large scatter in the values of this ratio.

Another way of comparing the proton numbers is to calculate the precipitation fraction, reported in Figure 8 by event number. This is the fraction $N_{\rm LDGRF}/(N_{\rm LDGRF}+N_{\rm SEP})$ of the total number of protons accelerated (those that escape as SEPs plus those that produce the LDGRFs) that would have to precipitate to account for the LDGRFs. For five events, only a relatively small fraction of particles ($\lesssim$3%) are required to precipitate back to the Sun, while for the rest of the sample, the fraction is larger than 10%, with three events that require $\gtrsim$83% to precipitate back to the Sun. We conclude that the large fraction of precipitating protons required to explain the LDGRF emission in several of the events surveyed and the lack of any pattern in the ratio of $N_{\rm LDGRF}$ over the sum of $N_{\rm LDGRF}$ and $N_{\rm SEP}$ pose significant challenges to the CME-driven shock scenario as the source of LDGRF emission.

4.3. Uncertainties on the SEP Propagation Axis

In Section 3, we assumed that the latitudinal angle of the SEP spatial distribution peak coincides with the latitude of the parent flare ($\alpha_{\rm sep}=\alpha_{\rm flare}$). However, the SEP propagation axis can be more closely associated with the related CME direction. The CME may also be launched nonradially above the active region's core or deflected, for example, by coronal holes, with significant implications in terms of latitudinal connectivity (Gopalswamy & Mäkelä 2014; Gopalswamy et al. 2014). We estimated the effect of the above approximation on $N_{\rm SEP}$ by comparing the derived SEP distributions with those obtained by using the CME directions from DONKI (see column 11 in Table 1) in place of flare locations ($\alpha_{\rm sep}=\alpha_{\rm cme}$). The resulting differences in the Gaussian fit parameters ($\beta_{\rm sep}$ and σ) are both $\lesssim$3.6°, while the resulting variations in $N_{\rm SEP}$ are $\lesssim$27%, with the exception of the 2012 January 27 event, for which the $N_{\rm SEP}$ value is ∼47% larger. This is likely due to the relatively large (13°) discrepancy between $\alpha_{\rm cme}$ and $\alpha_{\rm flare}$. The SEP distributions were also compared with those computed by using the CME flux rope directions from Gopalswamy et al. (2014, 2015). In this case, the variations in the $\beta_{\rm sep}$ and σ

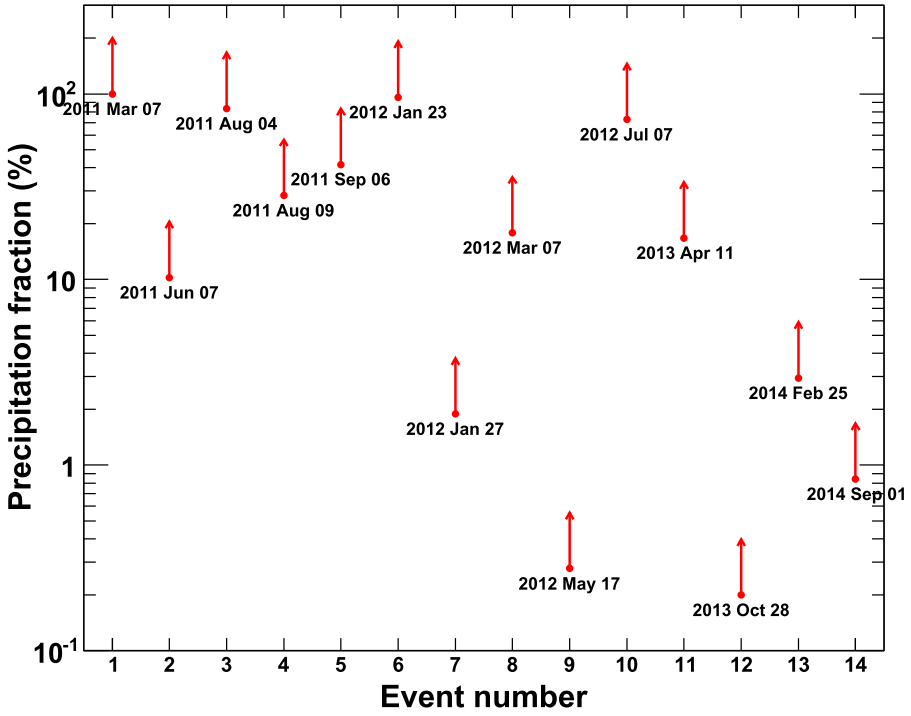

Figure 8. Lower limits on the fraction of precipitating protons $N_{\rm LDGRF}/(N_{\rm SEP}+N_{\rm LDGRF})$.

parameters are $\lesssim$1.5° and $\lesssim$0.6°, respectively, and an ∼15% maximum difference is found for the corresponding $N_{\rm SEP}$ values. These results suggest that uncertainties in the latitudinal angle of the SEP spatial distribution peak are not expected to significantly affect the comparison between the $N_{\rm SEP}$ and $N_{\rm LDGRF}$ values.

4.4. Comparison with Previous Works

An estimate of the number of SEPs at 1 au has also been provided by Share et al. (2018) for some events in common with the present analysis. Comparison of these SEP numbers is complicated by the fact that the adopted approaches are significantly different in terms of the derived SEP spatial distribution, transport effects, and data sets studied. In particular, Share et al. (2018) assumed, for all considered SEP events, a Gaussian distribution derived by combining the neutron monitor observations of 57 GLE events. The neutron monitor data for two GLE observations were also used to derive the number of 1 au crossings, which was found to be much lower ($\overline{N}_{\rm cross}=2$) than those evaluated in this work. Furthermore, Share et al. (2018) used *GOES*/HEPAD proton data with a less accurate calibration scheme than that used here. Moreover, these data were fit with a pure power-law function, neglecting the high-energy spectral rollovers reported by the *PAMELA* experiment (Bruno et al. 2018), and this results in a large overestimate of particle intensities above 500 MeV. As a consequence, the corresponding SEP proton numbers estimated by Share et al. (2018) are, on average, a factor of ∼20 larger than those evaluated in this work.

5. Discussion

One of the prominent explanations for the extended duration of LDGRFs is continuous back precipitation of energetic protons accelerated at a CME-driven shock as it propagates outward from the Sun. In this model, both the LDGRF and 1 au SEP signatures are due to protons drawn from the same population. However, because of the strong mirroring effect impeding the transport of protons back to the Sun (Hudson 2017), this scenario would require $N_{\rm SEP}$ to be significantly larger than $N_{\rm LDGRF}$. The picture that emerges from our analysis is not consistent with a source rooted in back precipitation from CMEs. For example, even with large systematic uncertainties, the 2012 May 17 event misses the equality line in Figure 7 by a factor of $\sim10^3$ in γ-ray-producing protons, and it differs from the 2012 March 7 event by a factor of $>10^3$ for a similar integrated particle number at 1 au. This could be explained by the likely sporadic and unpredictable magnetic connection between the shock front and the Sun. Nevertheless, it would follow that the intensity time profile in any given LDGRF would be similarly wildly varying, atypical of most well-measured LDGRFs observed by *Fermi*/LAT.

The events to the upper left of the equality are doubly problematic because they represent events where the particle number at the flare exceeds, sometimes considerably, the particle number in space. The implications of this pose a serious challenge to theory. If the particles above 500 MeV in space were from the same population as those responsible for the γ-ray emission at the Sun, it would imply that in some cases, more than ∼80% of this population must be extracted from the acceleration process to produce the γ radiation. In particular, although the estimate of $N_{\rm SEP}$ is subject to large uncertainties related to multiple injections, the number of protons inferred from the *Fermi*/LAT detection during the 2011 March 7 event, associated with the second-longest duration γ-ray emission, is more than 4 orders of magnitude larger. Losses of this magnitude from the shock would certainly quench the particle acceleration process long before particles of sufficient energy and number could be produced by the shock. Furthermore, because the shock formation height estimated for the 2011 March 7 and 2012 January 23 events is relatively large (∼2 R_s; Gopalswamy et al. 2013; Joshi et al. 2013), the

challenge to get particles back from a weakening shock to the Sun is even greater.

The problem is exacerbated for events such as those of 2012 March 7 and 2014 February 25 because the SEP spectra fall off exponentially above a few hundred MeV (Bruno et al. 2018), while there are abundant γ-rays exceeding 1 GeV from the flare (Share et al. 2018). Consequently, a particle number plot similar to that for Figure 7, but for higher energies, would push the points much farther upward and to the left of an equality line, aggravating the problem. Although CME-driven shock protons exhibit a prolonged, delayed, and high-energy behavior, we find it difficult to reconcile the back-precipitation scenario with the production of the high-energy γ radiation at the Sun because it seems to badly fail the total particle number test, implying a separate process associated with the CME only in a general order-of-magnitude sense, consistent with the trend in the data.

Complications arise in other ways, in particular from two *Fermi*/LAT detections on 2012 October 23 and 2012 November 27 that were not linked to CME eruptions, suggesting that a fast CME is not a necessary requirement of LDGRFs. In addition, while it has been shown that many bright X-ray flares are not associated with LDGRFs (Winter et al. 2018), there are also counterexamples of very fast front-side CMEs that were not accompanied by >100 MeV γ-ray emission, such as the two full halo CMEs observed at 10:48 UT on 2011 September 22 (1905 km s^{-1}) and 12:48 UT on 2011 September 24 (2018 km s^{-1}) and the partial halo CME registered at 03:12 UT on 2013 June 21 (1900 km s^{-1}). Similarly, while all reported LDGRFs are associated with impulsive-flare hard X-rays with energies above 100 keV, the latter is not a sufficient condition for the production of LDGRFs (Share et al. 2018). Finally, no long-duration γ-ray observation was reported by *Fermi*/LAT during the two front-side eruptions producing >500 MeV SEPs measured by *PAMELA* on 2012 March 13 and 2012 July 8. However, firm conclusions about the absence of >100 MeV γ-ray emission in such events are complicated by the limited duty cycle of the LAT when viewing the Sun.

An alternative to back precipitation is the scenario where particles are accelerated via second-order Fermi mechanism and trapped locally within extended coronal loops, after which (or concurrently) they diffuse to the denser photosphere to radiate (Ryan & Lee 1991). The favorable conditions can be provided by the magnetic structures appearing during the gradual phase of two-ribbon flares and CME liftoff, as field line reconnection gives rise to hot flare loops whose size can exceed 1 R_s, creating a system of arches that can persist for several hours. Based on observations of gyrosynchrotron (GS) emission from the Nancay Radioheliograph (NRH), Grechnev et al. (2018) provided evidence that the behind-the-limb flare of 2014 September 1 involved two distinct quasi-static loops, one that is associated with an initial hard X-ray flare and another, larger one associated with a second hard X-ray flare. Comparing these observations with simulations, they noted that the time profiles of the GS, hard X-ray, and, to some extent, >100 MeV γ-ray emission from *Fermi*/LAT of the latter microwave source are consistent with prolonged confinement (and perhaps reacceleration) of particles injected within a magnetic trap.

A compelling association of a large, extended loop with >100 MeV γ-ray emission is also provided by recent microwave observations from EOVSA (Gary et al. 2018). During the 2017 September 10 solar eruption that produced a GLE and an LDGRF, EOVSA microwave observations identified the footpoints of a large coronal loop with a circular length of ~1.4 R_s. The microwave emission persisted well into the extended phase of the >100 MeV γ-ray emission. The robust and smooth exponential decay of the latter argues for the coronal trap scenario, with spatial and momentum diffusion governing the precipitation of high-energy particles (Ryan et al. 2018b), as seen in every other well-measured LDGRF (Share et al. 2018). This approach conveniently decouples the acceleration of the γ-producing particles from the acceleration and transport of the SEPs, which, in turn, allows for different spectral shapes, as well as different energetic particle productivities, as seen in this analysis. The intrinsic prolonged durations of the γ-ray signatures from both processes speak to the large requisite spatial scales for both processes and the resulting high energies. Because the loop scenario is local and diffusive in nature, it would naturally produce smooth exponential decays, since no sequence of magnetic connects or disconnects would occur, as would be expected for a propagating large-scale feature like a CME.

A problem encountered in more widespread acceptance of this scenario is that although large loop structures ($\gtrsim$1 R_s) are common, they are often difficult to visualize, not filled with hot plasma or enough 100 keV electrons to be visible in soft X-ray or radio emission. For the purpose of accelerating protons, only magnetic turbulence or Alfvén waves are necessary with $\delta B/B \sim 10\%$ (Ryan et al. 2018a). New radio observations can help to place constraints on loop size and the ambient conditions within the loop that will improve future modeling of LDRGFs within the context of the continuous acceleration and trapping scenario.

6. Summary

Taking advantage of the unique high-energy observations from *PAMELA*, we conducted the first direct comparison of the number of interacting protons at the Sun and the number of SEP protons in the energy range above the ~300 MeV pion production threshold. Several key factors contribute to the analysis, including the ability to obtain SEP energy spectra up to a few GeV, firmly establishing spectral rollovers for all high-energy SEP events observed (Bruno et al. 2018). In particular, we calculate the total number of >500 MeV protons at 1 au by combining *PAMELA* and *STEREO* data with the aid of transport simulations and compare it with the number of high-energy protons at the Sun, as deduced from *Fermi*/LAT data (Share et al. 2018). The results of our analysis show that the two proton numbers are uncorrelated such that their ratio spans more than 5 orders of magnitude. The lack of correlation, and in particular, several extreme cases where the number of protons required to account for LDGRFs far exceeds the number of SEP protons, suggests that the LDGRF emission is probably not due to the back precipitation of particles accelerated at CME-driven shocks. Moreover, as demonstrated by the two LDGRF events occurring on 2012 October 23 and November 27, the association with fast CMEs does not appear to be a necessary requirement for high-energy γ-ray emission. In fact, while bright flares and impulsive >100 keV hard X-rays are not sufficient conditions for LDGRFs, there also several counterexamples of fast halo CMEs that were not accompanied by >100 MeV γ-ray emission, though the limited

exposure of the LAT instrument complicates the interpretation. An alternative explanation for LDGRFs based on continuous particle acceleration and trapping within large coronal structures that are not causally connected to the CME shock is discussed, and new remote observations of these loops, such as those provided by EOVSA, may help to constrain the role of such acceleration in producing LDGRF emission.

The authors thank the *ACE*, *GOES*, and *STEREO* teams for making their data publicly available. G.A. de N. acknowledges support from Fermi/GI grant NNH10ZDA001N-FERMI, NASA/HSR grant NNH13ZDA001N-HSR, and NASA/ISFM grant HISFM18. A.B. acknowledges support by an appointment to the NASA postdoctoral program at the NASA Goddard Space Flight Center, administered by Universities Space Research Association under contract with NASA. S.D. acknowledges support from the UK Science and Technology Facilities Council (STFC; grant ST/R000425/1). J.G. acknowledges support from NASA grant NNX15AJ 71G and NSF grant 1735422. I.G.R. acknowledges support from NASA Living With a Star grant NNG06EO90A.

ORCID iDs

G. A. de Nolfo https://orcid.org/0000-0002-3677-074X
A. Bruno https://orcid.org/0000-0001-5191-1662
J. M. Ryan https://orcid.org/0000-0003-3534-5968
S. Dalla https://orcid.org/0000-0002-7837-5780
I. G. Richardson https://orcid.org/0000-0002-3855-3634
E. R. Christian https://orcid.org/0000-0003-2134-3937
S. J. Stochaj https://orcid.org/0000-0001-6476-7524
M. Martucci https://orcid.org/0000-0002-3033-4824

References

Ackermann, M., Ajello, M., Albert, A., et al. 2013, ApJ, 771, 57
Ackermann, M., Ajello, M., Albert, A., et al. 2014, ApJ, 787, 15
Ackermann, M., Ajello, M., Allafort, A., et al. 2012, ApJ, 745, 144
Ackermann, M., Allafort, A., Baldini, L., et al. 2017, ApJ, 835, 219
Adriani, O., Barbarino, G. C., Bazilevskaya, G. A., et al. 2011, ApJ, 742, 102
Adriani, O., Barbarino, G. C., Bazilevskaya, G. A., et al. 2014, PhR, 544, 323
Adriani, O., Barbarino, G. C., Bazilevskaya, G. A., et al. 2017, NCim, 10, 473
Afanasiev, A., Battarbee, M., & Vainio, R. 2015, A&A, 584, A81
Ajello, M. A. A., Allafort, A., Baldini, L., et al. 2014, ApJ, 789, 20
Akimov, V. V., Belaoussov, A. S., Blokhintsev, I. D., et al. 1991, ICRC (Dublin), 3, 73
Akimov, V. V., Afanassyey, V. G., Belaousov, A. S., et al. 1996, SoPh, 166, 107
Aschwanden, M. J., Caspi, A., Cohen, C. M. S., et al. 2017, ApJ, 836, 17
Atwood, W. B., Abdo, A. A., Ackermann, M., et al. 2009, ApJ, 697, 1071
Battarbee, M., Dalla, S., & Marsh, M. S. 2018, ApJ, 854, 23
Berezhko, E. G., & Taneev, S. N. 2003, AstL, 29, 530
Bruno, A. 2017, SpWea, 15, 1191
Bruno, A., Adriani, O., Barbarino, G. C., et al. 2016a, AdSpR, 60, 788
Bruno, A., Adriani, O., Barbarino, G. C., et al. 2016b, JPhCS, 675, 032006
Bruno, A., Bazilevskaya, G. A., Boezio, M., et al. 2018, ApJ, 862, 97
Bruno, A., Christian, E. R., de Nolfo, G. A., Richardson, I. G., & Ryan, J. M. 2019, SpWea, 17, 419
Cane, H. V., McGuire, R. E., & von Rosenvinge, T. T. 1986, ApJ, 301, 448
Cane, H. V., Reames, D. V., & von Rosenvinge, T. T. 1988, JGR, 93, 9555
Chollet, E. E., Giacalone, J., & Mewaldt, R. A. 2010, JGR, 115, A06101
Chupp, E. L., & Ryan, J. M. 2009, RAA, 9, 11
Cliver, E. W. 1989, SoPh, 122, 319
Cliver, E. W. 2016, ApJ, 832, 128
Cliver, E. W., Kahler, S. W., Neidig, D. F., et al. 1995, ICRC (Rome), 4, 257
Cliver, E. W., Kahler, S. W., & Vestrand, W. T. 1993, ICRC (Calgary), 3, 91
Cliver, E. W., Nitta, N. V., Thompson, B. J., et al. 2005, SoPh, 225, 105
Cohen, C. M. S., Mason, G. M., & Mewaldt, R. A. 2017, ApJ, 843, 132
Dalla, S., & Agueda, N. 2010, in AIP Conf. Proc. 1216, Twelfth International Solar Wind Conference, ed. M. Maksimovic, K. Issautier, & N. Meyer-Vernet (Melville, NY: AIP), 613
Desai, M., & Giacalone, J. 2016, LRSP, 13, 3
Forrest, D. J., Vestrand, W. T., Chupp, E. L., et al. 1985, ICRC, 4, 146
Gary, D. E., Chen, B., Dennis, B. R., et al. 2018, ApJ, 863, 83
Gopalswamy, N., & Mäkelä, P. 2014, in ASP Conf. Ser. 484, Outstanding Problems in Heliophysics: from Coronal Heating to the Edge of the Heliosphere, ed. Q. Hu & G. Zank (San Francisco, CA: ASP), 63
Gopalswamy, N., Mäkelä, P., Akiyama, S., et al. 2014, ApJ, 806, 8
Gopalswamy, N., Mäkelä, P., Yashiro, S., et al. 2015, JPhCS, 642, 012012
Gopalswamy, N., Mäkelä, P., Yashiro, S., et al. 2017, JPhCS, 900, 012009
Gopalswamy, N., Mäkelä, P., Yashiro, S., et al. 2018, ApJL, 868, L19
Gopalswamy, N., Xie, H., Mäkelä, P., et al. 2013, AdSpR, 51, 1981
Grechnev, V. V., Kiselev, V. I., Kashapova, L. K., et al. 2018, SoPh, 293, 133
Hudson, H. S. 2017, in IAU Symp. 335, Space Weather of the Heliosphere: Processes and Forecasts, ed. C. Foullon & O. E. Malandraki (Cambridge: Cambridge Univ. Press), 49
Janardhan, P., Fujiki, K., Ingale, M., et al. 2018, A&A, 618, A148
Jin, M., Petrosian, V., Liu, W., et al. 2018, ApJ, 867, 122
Joshi, N. C., Uddin, W., Srivastava, A. K., et al. 2013, AdSpR, 51, 1981
Kahler, S. W., Sheeley, N. R., Jr, Howard, R. A., et al. 1984, JGR, 89, 9683
Kanbach, G., Bertsch, D. L., Fichtel, C. E., et al. 1993, A&AS, 97, 349
Kocharov, L., Laitinen, T., Vainio, R., et al. 2015, ApJ, 806, 80
Laitinen, T., Effenberger, F., Kopp, A., & Dalla, S. 2018, JSWSC, 8, A13
Lario, D., Aran, A., Gomez-Herrero, R., et al. 2013, ApJ, 767, 41
Lario, D., Kallenrode, M.-B., Decker, R. B., et al. 2006, ApJ, 653, 1531
Lario, D., Kwon, R.-Y., Richardson, I. G., et al. 2017, ApJ, 838, 51
Lario, D., Roelof, E. C., & Decker, R. B. 2014, in ASP Conf. Ser. 484, Outstanding Problems in Heliophysics: From Coronal Heating to the Edge of the Heliosphere, ed. Q. Hu & G. P. Zank (San Francisco, CA: ASP), 98
Lee, M. A. 2005, ApJS, 158, 38
Litvinenko, Y. C. 2006, A&A, 452, 1069
Mandzhavidze, N., & Ramaty, R. 1992, ApJ, 389, 739
Marsh, M. S., Dalla, S., Kelly, J., & Laitinen, T. 2013, ApJ, 774, 4
Mason, G. M., Gloeckler, G., & Hovestadt, D. 1984, ApJ, 280, 902
Mewaldt, R. A., Cohen, C. M. S., Giacalone, J., et al. 2008, in AIP Conf. Proc. 1039, Particle Acceleration and Transport in the Heliophere and Beyond, ed. G. Li et al., 111
Mewaldt, R. A., Cohen, C. M. S., Mason, G. M., et al. 2013, in AIP Conf. Proc. 1539, Solar Wind, ed. G. P. Zank (Melville, NY: AIP), 116
Miteva, R., Samwel, S. W., & Krupar, V. 2017, JSWSC, 7, A37
Murphy, R. J., Dermer, C. D., & Ramaty, R. 1987, ApJS, 63, 721
Ng, C. K., & Reames, D. V. 2008, ApJL, 686, L123
Nitta, N. V., Aschwanden, M. J., Boerner, P. F., et al. 2013, SoPh, 288, 241
Palmer, I. D. 1982, RvGeo, 20, 335
Plotnikov, I., Rouillard, A. P., & Share, G. H. 2017, A&A, 608, A43
Ramaty, R., & Murphy, R. 1987, SSRv, 45, 213
Rank, G., Ryan, J. M., Debrunner, H., et al. 2001, A&A, 378, 1046
Reames, D. V. 1999, SSRv, 90, 413
Richardson, I. G., von Rosenvinge, T. T., Cane, H. V., et al. 2014, SoPh, 289, 3059
Richardson, I. G., von Rosenvinge, T. T., Cane, H. V., et al. 2017, AdSpR, 60, 755
Ryan, J. M. 2000, SSRv, 93, 581
Ryan, J. M., de Nolfo, G. A., et al. 2018a, in Solar Heliospheric & Interplanetary Environment (SHINE) Conf. (Arlington, VA: The National Science Foundation), 134
Ryan, J. M., de Nolfo, G. A., & Gary, D. E. 2018b, AGUFM, SH51C-2829
Ryan, J. M., & Lee, M. A. 1991, ApJ, 368, 316
Sandberg, I., Jiggens, P., Heynderickx, D., et al. 2014, GeoRL, 41, 4435
Schneid, E. J., Brazier, K. T. S., Kanbach, G., et al. 1994, in AIP Conf. Proc. 294, High-energy Solar Phenomena, ed. J. Ryan & W. T. Vestrand (Melville, NY: AIP), 94
Share, G. H., Murphy, R. J., Tolbert, A. K., et al. 2018, ApJ, 869, 182
Tan, L. C., Reames, D. V., Ng, C. K., et al. 2009, ApJ, 701, 1753
Thakur, N., Gopalswamy, N., Xie, H., et al. 2014, ApJL, 790, L13
Van Hollebeke, M. A. I., Ma Sung, L. S., & Mcdonald, F. B. 1975, SoPh, 41, 189
Winter, L. M., Bernstein, V., Omodei, N., et al. 2018, ApJ, 864, 39
Zank, G. P., Li, G., Florinski, V., et al. 2006, JGR, 111, A06108
Zank, G. P., Rice, W. K. M., & Wu, C. C. 2000, JGR, 105, 25079